ResearchGate

See discussions, stats, and author profiles for this publication at: https://www.researchgate.net/publication/319558026

High Angular Resolution Diffusion Imaging (HARDI)

Chapter · June 2015

DOI: 10.1002/047134608X.W8258

CITATIONS
14

READS
2,726

1 author:

Maxime Descoteaux
Université de Sherbrooke

295 PUBLICATIONS **5,119** CITATIONS

SEE PROFILE

Some of the authors of this publication are also working on these related projects:

Project High resolution diffusion weighted MRI View project

Project Surface-enhanced tractography View project

All content following this page was uploaded by Maxime Descoteaux on 19 October 2017.

The user has requested enhancement of the downloaded file.

HIGH ANGULAR RESOLUTION DIFFUSION IMAGING (HARDI)

1. INTRODUCTION

Diffusion magnetic resonance imaging (dMRI) is a unique noninvasive technique capable of quantifying the diffusion process of water molecules in *living* biological tissues like the human brain white matter. The great success of diffusion MRI comes from its capability to accurately describe the geometry of the underlying white matter axonal microstructure. Hence, diffusion MRI can map the structural organization of the white matter, also called white matter wiring, as seen in Figure 1.

Diffusion MRI also captures the local diffusion phenomenon of water molecules, which probes the structure of the biological tissues at scales much smaller than the imaging resolution. It can thus serve to recover information about cell sizes and axonal diameter, which has recently given birth to a new and exciting field of research on *diffusion microstructure*. Diffusion MRI is a vast field and hundreds of acquisition schemes and models exist. Here, we focus on high angular resolution diffusion imaging (HARDI), which is approximately 15 years old and now at the heart of a large number of neuroscience research studies and several clinical applications on human brain mapping.

This article will therefore cover the young history of HARDI, from basic diffusion principles and diffusion tensor imaging to q-space imaging (QSI), HARDI, and beyond with a review of the latest advanced reconstruction techniques. The reader will be taken through a historical progression of the field. State-of-the-art techniques as well as their limitations and the questions that are still open will be described. Some clinical applications will be highlighted throughout the article wherever possible. Note that this article is aimed at readers new to the field of diffusion MRI or are pursuing a graduate program. The article is also written more from the viewpoint of *image processing* than from the traditional *physics* viewpoint. HARDI techniques can quickly become mathematically involved. Appropriate intuitions and a large number of references are given for the curious reader to refer to for obtaining greater details on the topic.

2. PRINCIPLES OF DIFFUSION

In liquids and gas, the molecules follow a random motion resulting in mechanical collisions between molecules that yield abrupt and random modifications in their motion direction. Figure 2 illustrates a very simple experiment in which a drop of blue ink was placed on two different paper types: (i) tissue paper and (ii) newspaper.

In tissue paper, after a certain amount of time, the ink spreads all over the tissue paper nearly equally likely in all directions. This is because tissue paper is a very soft paper to not give a rash to our nose. Its microstructure is much smaller than the size of ink particles and so the ink particles do not face important obstacles in their way, just as if it was placed inside a glass of water. Diffusion is free and is said to be *isotropic*. On the contrary, newspaper is a very rough and structured paper. Hence, after the same time, the blue ink tends to follow the structure of the paper more easily leading to a typical nonisotropic pattern called *anisotropy*. This pattern of anisotropy reflects the geometry of the underlying structure in the paper. This simple experiment is characteristic of the underlying microscopic process that physicists call the *diffusion process*, which is at the heart of diffusion MRI. We will use observations of this diffusion process as an indirect way to infer information about the underlying microstructure.

Back in 1827, the botanist Robert Brown was the first to observe the random motion of pollen grains in water, giving his name *Brownian* motion (1) to such free motion due to shocks between particles. In 1905, Einstein published a seminal paper demonstrating that the Brownian motion of a particle in a fluid is characterized by a *diffusion coefficient* D in $\mathrm{mm}^2\,\mathrm{s}$, which is related to the root mean square displacement $\langle R\rangle$ in any direction after a time t (2):, $\langle \mathrm{R}\rangle = 2nD{\cdot}t$, where n is the number of dimensions considered (for 3D, $\langle R\rangle = 6D{\cdot}t$). In the case of free diffusion (without any obstacles), the probability distribution function of the motion $p(\mathbf{r}, t)$ (also called the *diffusion propagator*) of any particle starting from the origin and observed at the position $\boldsymbol{r}$ after a diffusion time t is Gaussian or a *Normal* distribution:

$$p(\mathbf{r}, t) = \frac{1}{\sqrt{(4\pi t)^3 D}} \exp\left(-\frac{\mathbf{r}^T\mathbf{r}}{4tD}\right) \tag{1}$$

This Gaussian property remains true only in the case of a boundless and free environment. Without obstacles hindering or restricting the diffusion process, molecules do not follow any preferential direction and move along all the directions of the 3D space with the same likelihood such as in the tissue paper experiment of Figure 2. This is unfortunately not preserved in tissues where the media is bounded and where cell membranes hinder or restrict the motion of molecules (3). This is when anisotropic diffusion is observed, as in the newspaper experiment of Figure 2.

In the human brain, the situation is similar but now the white matter consists of large bundles of parallel fibers interconnecting the various functional areas of the cortex and the deep gray matter structures. The geometry of white matter bundles can be roughly represented by cylinders. The behavior of water molecules in the human brain is thus strongly dependent on the environment of their surrounding membranes, and their motion is subject to distinct phenomena. On one end, membranes form boundaries that restrict the motion of molecules inside cells, leading to a diffusion coefficient being lower than the free diffusion coefficient in an unbounded media, similar to the newspaper experiment of Figure 1. Hence, diffusion is no longer *free*, which is why we often use the term apparent diffusion coefficient (ADC) for water molecules trapped in brain tissue, as opposed to the Einstein's diffusion coefficient D in free water.

J. Webster (ed.), *Wiley Encyclopedia of Electrical and Electronics Engineering*. Copyright © 2015 John Wiley & Sons, Inc.
DOI: 10.1002/047134608X.W8258

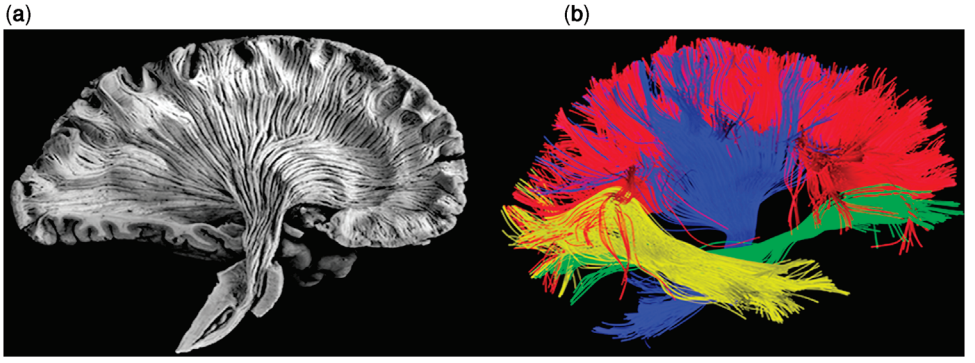

Figure 1. White matter bundles and tractography preview. (a) Dissection of a human brain (The Virtual Hospital) highlighting the white matter connectivity made up of axonal fibers. (b) Artistic rendering of a bundle of fibers and of the trajectories of water molecules moving along or across the bundle.

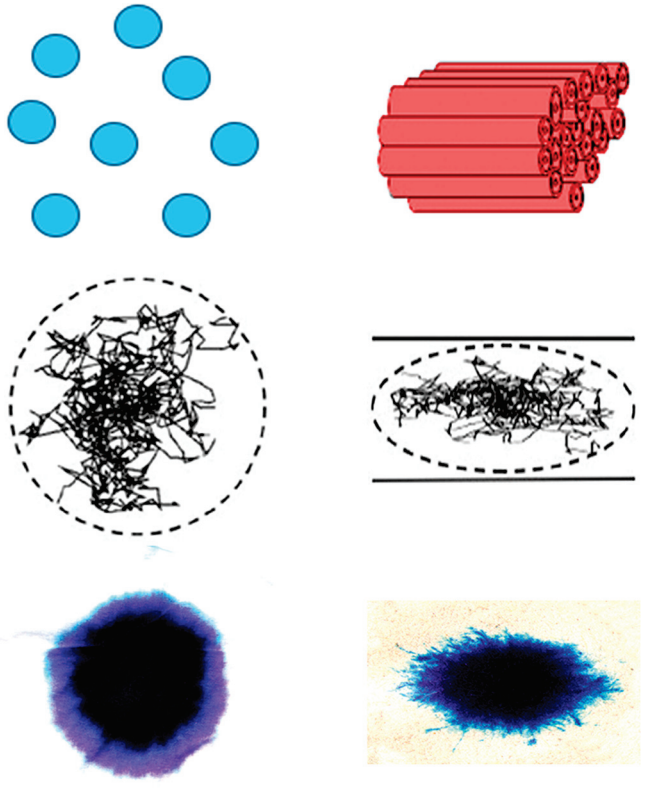

Figure 2. Brownian motion, isotropy, and anisotropy. Drop of ink diffusing on soft tissue paper and newspaper. Anisotropy of the diffusion process in a porous media. In brain tissues, the membranes of axons restrict the diffusion process, yielding a diffusion pattern depicting a larger free average displacement along the main direction of the axons than across; as a consequence, the anisotropy of the diffusion process of water molecules inside the porous media provides information about its geometry.

3. IMAGING DIFFUSION

It is beyond the scope of this article to get into the physics of diffusion MRI. Several good chapters exist on the subject (4, 5). It is an important topic because diffusion MRI acquisition is challenging and producing high-quality raw diffusion MRI is all about the physics of the acquisition and dealing with imperfections of the diffusion sequences. An intuitive image processing view will be given of the basic principles of diffusion imaging for HARDI reconstruction.

Measuring diffusion using MRI is in fact the story of transforming an MRI defect or artefact into a powerful tool. This defect is the dephasing of spins caused by moving particles. In fact, Brownian motion is responsible for small dephasing of spins, which causes a slight decrease of the measured MRI signal magnitude. In 1965, Stejskal and Tanner wrote their pioneer paper after understanding the potential of this signal attenuation to probe the motion of molecules inside tissue samples and compute the apparent diffusion coefficient and proposed a novel pulsed-gradient spin echo MR sequence (6). This sequence remains, as of today, a standard scheme to sensitize the MRI signal to diffusion.

Le Bihan introduced the b-value (for Bihan), which is one of the key parameters in diffusion imaging. The diffusion attenuation is tuned by the b-value and is measured in s/mm^2. Hence, mathematically, $b{\cdot}D$ in equation 2 is unit free. Today, it is still very important to set this b-value properly at the imaging console when acquiring the images. This b-value depends on γ, the gyromagnetic ratio of the water proton H^+, the diffusion time t during which the water molecules diffuse, and $|\boldsymbol{G}|$ is the diffusion gradient strength. Because of the limited hardware in human imaging and limited possibilities to administer heat on the human subject, the MRI machine gradient strength $|\boldsymbol{G}|$ is often maxed out, which effectively leaves the MR physicist only the diffusion time to play with to change the b-value.[1] Gradient $\boldsymbol{G}$ allows to navigate not only in 3D image frequency space (also called k-space) but also in 3D diffusion space, also called q-space. $\boldsymbol{q}$ is thus the frequency wave vector with norm in mm^{-1} units, $\mathbf{q} = \gamma\delta\ \mathbf{G}/2\pi$, and its relation with the b-value thus is $b = 4\pi^2\theta^2\tau$, where $t = \Delta - \delta/3$, δ is the time of the applied diffusion-sensitizing gradients, and Δ is the time between the two pulses. Hence, the diffusion signal can be expressed in terms of q or in terms of b. For now, we will only consider the diffusion signal in terms of b-value.

[1] Diffusion time t is still a relatively ignored parameter in general diffusion imaging experiments and only nuclear MR or more recently microstructure imaging applications are using it as a proper contrast parameter.

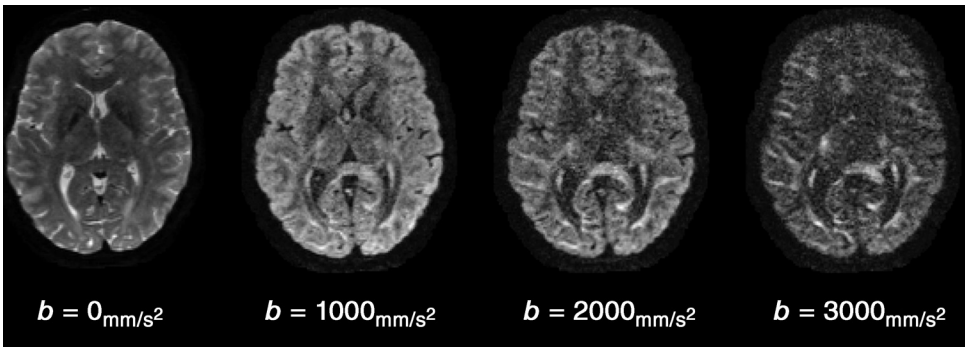

Figure 3. Diffusion signal depends on b-value. We see $b = 0$ (S_0) image and $b = 1000$, 2000, and 3000 s/mm^2 images. We note the signal attenuation as a function of b-value. Here, the data set chosen is from the Human Connectome Project public database. Images are in axial view. The gradient directions at each b-value are not exactly the same but are similar. The $b = 1000$ s/mm^2 image is for the 10th gradient direction $\mathbf{g} = [-0.219605, 0.890535, 0.398399]$, $b = 2000$ s/mm^2 image for the 262nd gradient direction $\mathbf{g} = [-0.328114, 0.914801, 0.235542]$, and $b = 3000$ s/mm^2 image for the 69th gradient direction $\mathbf{g} = [-0.112375, 0.891432, 0.439]$.

In our context and for the purpose of diffusion imaging and HARDI, it is important to realize that the higher the b-value, the more you let water molecules to dephase or to be "sensitive" to their molecular displacement. This results in more signal attenuation. In fact, if you perform a diffusion acquisition experiment with varying b-value from $b = 0$ s/mm^2 to a maximal b-value, you will observe an exponential-like signal decay curve. A simplistic approach is to fit this curve with a monoexponential decay:

$$S(b) = S_0 \exp(-bD) \tag{2}$$

where S_0 is the baseline T2-weighted image without any diffusion weighting and D is the apparent diffusion coefficient (ADC). In fact, this relation was discovered experimentally plotting the diffusion signal as a function of b-value. The points on the plot seemed to form an exponential-like curve and when doing a log-plot, the points gave a straight line with slope given by the ADC, D. This decay of the diffusion MRI signal in the presence of diffusing water molecules clearly indicates that imaging the diffusion process is challenging in terms of signal-to-noise ratio (SNR), as the attenuation of the MR signal may be severe due to the presence of the exponential decay. This is clearly illustrated in Figure 3.

However, from equation 2, one sees that it does not show the orientation dependence of the diffusion signal. This equation is correct for free diffusion or diffusion in the tissue paper experiment, but for our newspaper experiment, we see that the apparent diffusion coefficient is different depending on the orientation. Water molecules are diffusing in 3D space and they will bump into structure in three dimension. Hence, depending on which direction you look into, the water molecules will not behave the same. In a sense, this means that the apparent diffusion coefficient depends on the orientation, ADC(θ, φ). Hence, equation 2 must be extended to take orientation into account.

In 1990, Moseley was the first to observe that the diffusion process was anisotropic in white matter (7). The diffusion of water molecules was inherently a tridimensional (3D) process and a single diffusion-weighted image provides information only about the diffusion process occurring along a specific direction of the q-space, as seen in Figure 4.

To overcome this limitation, it was proposed to use three diffusion images along three orthogonal diffusion directions (x, y, z) and a baseline image without diffusion, leading to images S_x, S_y, S_z, and S_0. One would then solve equation 2 three times with these images and take a geometric average to obtain a pseudo-ADC: $\langle \mathrm{ADC} \rangle = (\mathrm{ADC}_x + \mathrm{ADC}_y + \mathrm{ADC}_z)/3$. This apparent diffusion coefficient estimation is very simple and useful in the diagnosis of brain ischemia, observing that the ADC of water molecules decreases immediately following ischemia (7). Hence, pseudo-ADC diffusion imaging is still part of the portfolio of MRI used in clinical emergency.

In 1991, Douek et al. understood the potential of the anisotropy of the diffusion process depending on the orientation of the diffusion gradients in the 3D space to probe the orientation of anisotropic media, such as in white matter (8). It was clear that the diffusion process was a 3D phenomenon and that a mathematical framework was necessary to perform 3D diffusion imaging independent of the (x, y, z) axes.

4. DIFFUSION TENSOR IMAGING (DTI)

In 1992 and 1993, based on the fundamental discovery of Douek et al, Basser et al. proposed to use the diffusion tensor to model the intrinsic diffusion properties of biological tissues (9–11). Then, in 1994, the seminal journal papers were published (12, 13). The diffusion tensor (DT) is the extension of the scalar diffusion coefficient encountered earlier in equation 2. A diffusion tensor is nothing more than a 3×3 matrix that is symmetric and positive definite because by nature, the diffusion process is symmetric and positive. Hence, a diffusion tensor is mathematically written as

$$\mathbf{D} = \begin{pmatrix} D_{xx} & D_{xy} & D_{xz} \\ D_{xy} & D_{yy} & D_{yz} \\ D_{xz} & D_{yz} & D_{zz} \end{pmatrix} \tag{3}$$

If we let $\mathbf{g} = \mathbf{q}/|\mathbf{q}|$ represent a unit gradient direction, that is, $|\mathbf{g}| = 1$, as opposed to the more general $\mathbf{q}$, which is a general wave vector q-space with norm $|\mathbf{q}|$. Multiplying each side of this tensor $\mathbf{D}$ by $\mathbf{g}$ and playing with the

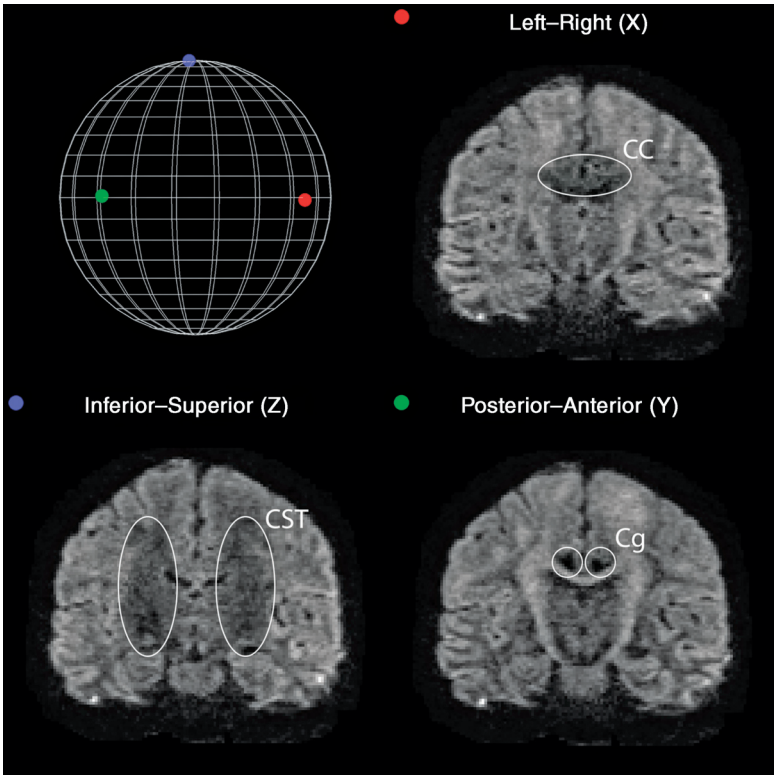

Figure 4. Diffusion signal depends on orientation. We see three diffusion-weighted images chosen in directions x, y, and z (red, green, and blue, respectively). Note how the contrast for different structures changes as function of orientation. Images are taken from the Human Connectome Project at $b = 1000\text{s/mm}^2$. Note how the corpus callosum, which is a structure orientated in the x-direction (left–right), is very dark and attenuated on the x-direction diffusion image. Similarly, the corticospinal tract, which is the motor white matter bundle orientated in the z-direction (inferior–superior), is also very dark and attenuated on the z-direction image, as opposed to the other two. This signal attenuation of diffusion MRI is important to understand and fully grasp. The more the structure aligned to the measured diffusion direction, the more attenuated the measured diffusion signal.

mathematics leads to the following equations:

$$\begin{aligned}\mathbf{g}^T\mathbf{D}\mathbf{g} &= (g_x\, g_y\, g_z)\begin{pmatrix} D_{xx} & D_{xy} & D_{xz} \\ D_{xy} & D_{yy} & D_{yz} \\ D_{xz} & D_{yz} & D_{zz}\end{pmatrix}\begin{pmatrix} g_x \\ g_y \\ g_z\end{pmatrix} \\ &= D_{xx}g_x^2 + D_{yy}g_y^2 + D_{zz}g_z^2 + 2D_{xy}g_xg_y \\ &\quad + 2D_{xz}g_xg_z + 2D_{yz}g_yg_z\end{aligned} \tag{4}$$

which is nothing more than the equation of an ellipse in three dimension, an ellipsoid, as illustrated in Figure 5. Positive definiteness means that $\mathbf{g}^T\mathbf{D}\mathbf{g} > 0$.

Since $\mathbf{D}$ is symmetric (equation 3), it has only six unknown coefficients to be estimated and leads to the extension of the scalar diffusion (eq. 2) to the 3D anisotropic version with the diffusion tensor equation:

$$S(\mathbf{g}, b) = S_0 \exp\left(-b\mathbf{g}^T\mathbf{D}\mathbf{g}\right) \tag{5}$$

Therefore, DTI needs at least six diffusion-weighted images and one S_0 to solve the system of equation 5. Typically, a b-value of 1000 s/mm^2 is used with 6–32 gradient directions ($\mathbf{g}$). The linear system of equation 5 is estimated using classical linear least-squares method or nonlinear least-squares (12). Simple examples of such reconstructions can be found in the diffusion imaging in python (Dipy, www.dipy.org, examples in the gallery). Hence, the reader must now realize that from

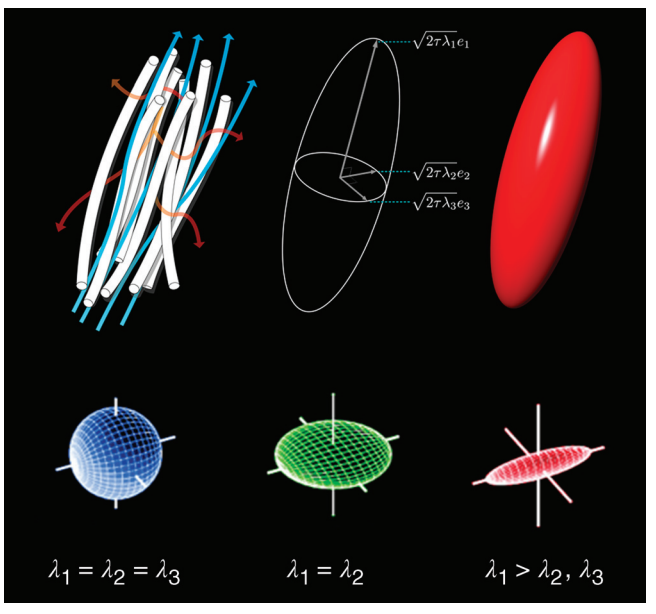

Figure 5. DTI ellipsoids, prolate, oblate, and spherical tensors. Water molecules diffusion along fibers. The diffusion tensor model captures this orientated diffusion process with the diffusion ellipsoid. Here, the FA of the illustrated tensor is approximately 0.7. The tensor can also be oblate if the first two eigenvalues are equal or spherical if all three are equal.

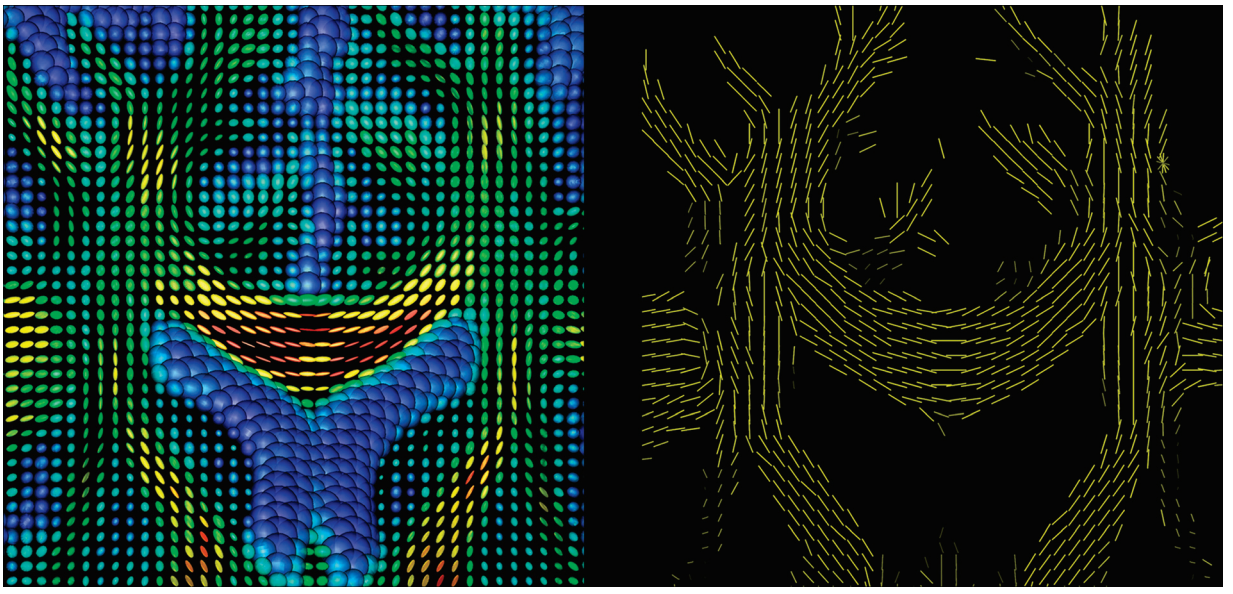

Figure 6. DTI principal direction and tractography. DTI produces an image of diffusion tensors or ellipsoids. The principal direction of these diffusion tensors aligned with the major white matter bundles. The diffusion tensor ellipsoids are colored according to their FA value, from blue to red, FA 0 to 1. Hence, spherical tensors are blue, oblate tensors are green, and prolate tensors are red, as shown in Figure 5.

N diffusion-weighted images of size $128 \times 128 \times 60$ (3D image of size X, Y, Z) measured along N different uniform orientations, that is, $\{S(\mathbf{g_1}, b), \ldots, S(\mathbf{g_N}, b)\}$, equation 5 is solved at every voxels. This results in a 4D image of size $128 \times 128 \times 60 \times 6$, where the last dimension contains the tensor coefficients $\{D_{xx}, D_{xy}, D_{xz}, D_{yy}, D_{yz}, D_{zz}\}$. In a sense, this is no longer a scalar image but what we call a tensor image or a tensor field, as seen in Figure 6. Numerous software allow the interactive visualization of such tensor fields, such as the FiberNavigator (https://github.com/scilus/fibernavigator).

From the diffusion tensor, one can perform an eigenvalue decomposition to diagonalize the tensor and obtain three eigenvalues and three eigenvectors that fully describe the geometric and diffusion properties of the tensor. Thus, the eigenvalue decomposition of the DT leads to the sorted eigenvalues λ_1, λ_2, λ_3, with $\lambda_1 \geq \lambda_2 \geq \lambda_3$, and corresponding eigenvectors $\boldsymbol{e}_1$, $\boldsymbol{e}_2$, $\boldsymbol{e}_3$. The largest eigenvalue λ_1 gives the principal direction of the DT, $\boldsymbol{e}_1$, and the other two eigenvectors span the orthogonal planes to it, as illustrated in Figure 5. This principal direction can also be visualized and followed to reconstruct major white matter bundles, as seen in Figure 6.

Hence, if the first eigenvalue is larger than the other two, we have a prolate tensor. If the first two eigenvalues are almost equal ($\lambda_1 = \lambda_2$), we have an oblate or a planar tensor, and if all three eigenvalues are almost equal ($\lambda_1 = \lambda_2 = \lambda_3$), we have a spherical tensor. Therefore, although a simple object, the tensor is rich and contains valuable tissue properties that depend on its eigenvalues and eigenvectors. One can thus define parallel and perpendicular diffusivity measures (14). Hence, linear, planar, and spherical measures can be extracted from the diffusion tensor (14), as illustrated in Figure 7.

Moreover, several rotationally invariant quantities can be extracted such as the trace of the DT, the apparent diffusion coefficient (ADC), or the fractional anisotropy (FA) (15), among others. These popular DTI measures are illustrated in Figure 7. The FA map is certainly the most famous DTI anisotropy measure. It is a normalized measure between 0 and 1 that lights up the white matter. The FA is a measure that tells us how far we are from a sphere or isotropic diffusion. High FA values (0.7 and more) reflect voxels with highly organized fiber bundles in a single direction, whereas low FA values (0.15 and lower) reflect voxels with isotropic diffusion. Mid-range FA

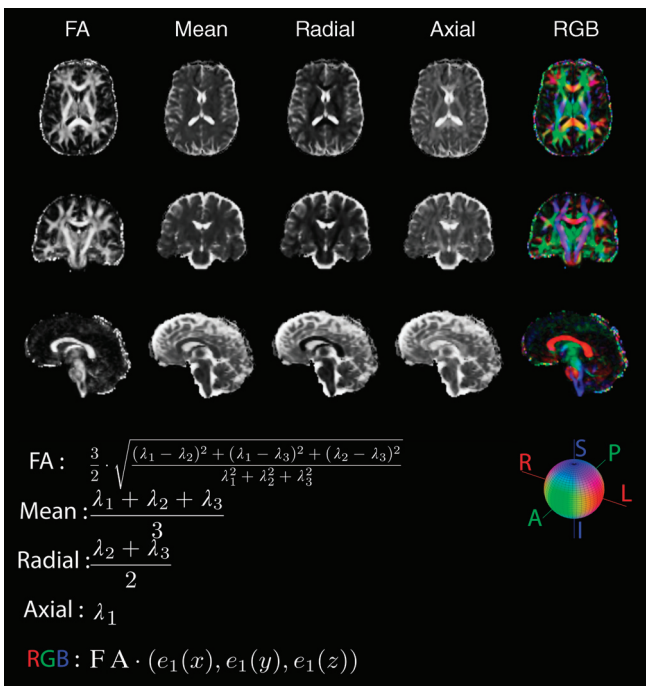

Figure 7. DTI measures. From the diffusion tensor and its eigenvectors and eigenvalues, several tissue measures or maps can be extracted such as the mean, axial, and radial diffusivities, fractional anisotropy (FA), and colored FA (RGB map). These measures are at the heart of numerous publications.

are much harder to interpret and can reflect several shapes between a sphere, a disk, or a fatter looking single tensor (see Figure 1 in Reference 16). It is thus important to observe that FA can be ambiguous, that is, it is possible that two tensors with different shapes produce the same FA values. Hence, other measures such as parallel (axial) and perpendicular (radial) diffusivities can be used to complement FA to separate diffusivity along the principal direction of the tensor and orthogonal directions. As seen in Figure 7, tensors can also be visualized as a colored FA map, where the red–green–blue (RGB) map encodes the left–right (LR), anterior–posterior (AP), inferior–superior (IS) directions of the principal eigenvector $\boldsymbol{e}_1$. The RGB map gives a good orientation representation of the DT field. One can also visualize the principal eigenvector or the ellipsoids themselves, as seen in Figure 6.

Hence, the diffusion tensor has powerful properties that one can exploit for diffusion MRI applications and clinical diagnosis (17–21), among many others. In fact, ADC, FA, parallel diffusivity, and perpendicular diffusivity maps are now a central part of several studies of neurological and pathological disorders (aging, Alzheimer's disease, brain tumors, diffusion axonal injury, dyslexia, dysplasia, epilepsy, HIV, Krabbe disease, multiple sclerosis, schizophrenia, stroke, vascular dementia, Wallerian degeneration, among others) (5). DTI acquisition, reconstruction, scalar maps, and basic streamline tractography are now part of every manufactured MRI system. This opens a large number of neuroscience applications. However, DTI is still not a "press button" procedure. Default parameters at the imaging console are not standard and are hard to select for the inexperienced user. Table 1 summarizes suggested DTI parameters for clinical use and research needs.

In summary, it is highly recommended to use isotropic voxels, long repetition time (TR), parallel imaging, a b-value in the range of 1000 s/mm^2, and as many directions as can fit in your clinical or research time window with, as a general rule of thumb, one $b = 0$ image (S_0) every 10 directions or so. As default parameters, many manufacturers select three averages or excitations (NEX) to increase the SNR. There are now powerful denoising techniques to increase SNR (22–27) and it is therefore suggested to measure more directions than do averaging, if time permits.

Table 1. Recommended Acquisition Parameter *Guide* for Clinical and Research DTI

Clinical DTI	Research DTI
$b = 1000$s/mm^2	$b = 1000$ s/mm^2
$N = 12$ directions	$N = 32$ directions (or more if time)
NEX = 3 (we suggest to use three times more directions or only 1 NEX)	NEX = 1
One to three $b = 0$ images (S_0) if possible	Three or more S_0 images
Long repetition time (TR) (~11 s)	Long repetition time (TR) (~11 s)
Parallel imaging ON	Parallel imaging ON
Isotropic voxels (2–2.3 mm isotropic)	Isotropic voxels ($1.8 \times 1.8 \times 1.8$ mm^3)
3–5 min	5–10 min

4.1. DTI Limitations

The most important limitation of the diffusion tensor model is its Gaussian diffusion model assumption. Hence, only a single-fiber population can be modeled at every imaging voxel. This is an important limitation when imaging voxels have multiple fiber populations crossing (28) or highly curving fiber bundle (29), as seen in Figure 8.

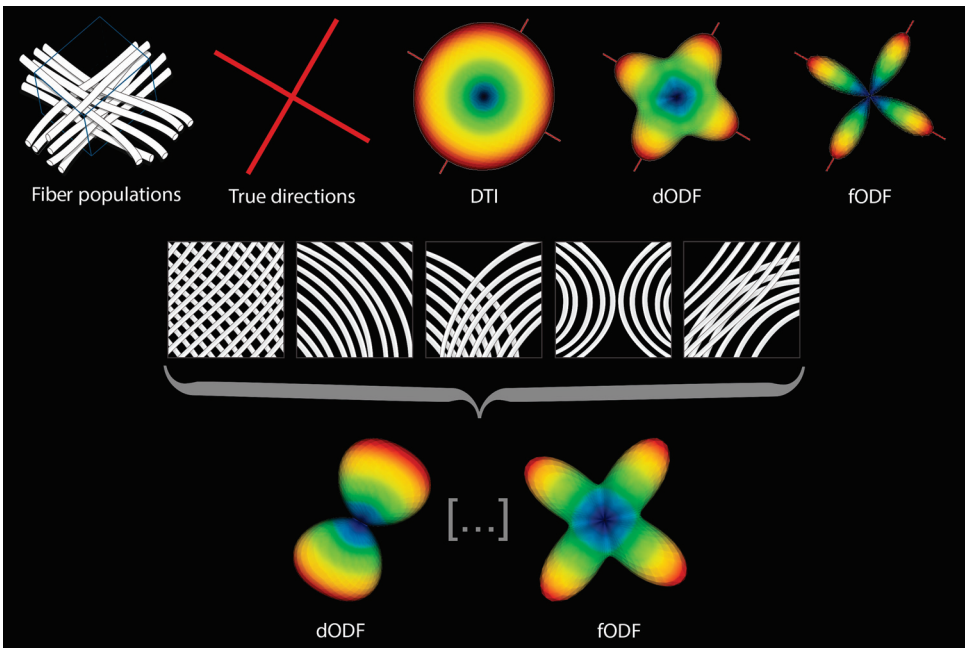

Figure 8. Crossing configurations. With a crossing configuration, we expect multiple peaks along each of the fiber population. However, the diffusion tensor is flat and limited. To overcome the limitations of DTI, we will need to reconstruct angular profiles that can capture the crossing fibers. Here, we see an orientation distribution function (ODF) and a fiber ODF. They will be detailed later. We also see that several ambiguous subvoxel configurations can lead to the same ODF or fiber ODF.

Table 2. Advantages and Limitations of DTI

DTI advantages	DTI disadvantages/ limitations
Short acquisition time (approximately 5 min)	
Available on most existing clinical system (acquisition, tensor reconstruction, scalar measures such as FA and ADC)	Limited in crossing and curving areas; only 1 fiber direction possible
Anisotropy measures (FA, parallel, perpendicular diffusivity) useful for clinical studies and aid for diagnosis	Scalar measures limited in non-Gaussian areas; measures must be interpreted with care

In these voxels, the tensor model is violated because diffusion in these voxels can no longer be modeled by a 3D Gaussian distribution. As mentioned before, this is an important problem, as at the current resolution of diffusion images (approximately 2 mm isotropic), it is estimated that between 66 and 90% of white matter, voxels with FA above 0.1 have multiple fiber crossing configurations (29, 30). In the worst case, this means that the DTI assumption is violated more than 2/3 of the time. If one is aware of DTI limitations and is careful as to how results are interpreted and used, it remains a powerful tool. Table 2 summarizes the key advantages and limitations of DTI.

Therefore, it is important to go beyond DTI. Higher order models and new reconstruction techniques are needed to be able to describe non-Gaussian diffusion signals. Of course, high-order models have more degrees of freedom and, therefore, more diffusion-weighted images will be required for the problem to be well defined and well posed. This has led to the development of HARDI techniques.

5. HIGH ANGULAR RESOLUTION DIFFUSION IMAGING (HARDI)

HARDI was originally developed to overcome the limitations of DTI and solve the *crossing fiber problem* to make tractography more robust and provide new anisotropy measures beyond the classical FA and diffusivities computed from DTI. Recall that the DTI estimation has six unknown coefficients to reconstruct, and thus a minimum of six diffusion-weighted images is required in addition to a baseline S_0 image. This is because a single 3D Gaussian distribution has six parameters, which can be parameterized by the diffusion tensor (eq. 3).

What is the natural extension to overcome the single Gaussian assumption? Why not try two Gaussians, three Gaussians, or N Gaussians? However, the more the Gaussians, the more unknowns to the estimate. The more the unknowns to the estimate, the more the diffusion measurements are needed. Do we need Gaussians anyway? Are there model-free techniques that can be used? All these questions gave birth to two families of techniques: (i) model-free techniques and (ii) model-based techniques. The common denominator of both families of techniques is that both more data and more sophisticated mathematics and optimization schemes are necessary for the reconstruction.

But what does it mean to need more data? What data and which diffusion measurements? More b-values, more directions, or both? This gave birth to the term *high angular resolution diffusion imaging*. The expression "HD-DTI" is often used in the media, for high-definition DTI because DTI is so well known and common. However, the "HD-DTI" expression can be misleading because the high definition is in terms of angular resolution, not spatial resolution. Also, an important requirement of HARDI is that it needs to be accompanied with *non-DTI* reconstruction techniques that will be covered in detail later. These non-DTI reconstruction techniques are the heart of HARDI and are often designed for a particular sampling and acquisition scheme. These reconstruction techniques are also quickly quite mathematically involved. New calculus is required to deal with mathematics on the sphere and advanced optimization methods are necessary to deal with noise and limited data.

The reader will be taken through a historical and an intuitive evolution of HARDI through model-free and model-based advanced 3D diffusion imaging techniques while introducing the necessary mathematics and reconstruction algorithms needed.

5.1. A Brief History of Advanced 3D Diffusion Imaging beyond DTI

Three-dimensional diffusion imaging and HARDI were introduced by the same group from work by Wedeen and Tuch at the turn of 2000 (31–34). The Ph.D. thesis of Tuch (34) is seminal and a *must-read* document for new students and new users in the field of diffusion MRI.

Advanced 3D diffusion imaging and HARDI highly depend on the acquisition scheme done. Hence, the first question to ask is what are the acquisition requirements? How do we measure and reconstruct this diffusion process? In the literature, HARDI is typically associated with spherical sampling schemes, but there also exists Cartesian, radial, and other sampling schemes in general 3D diffusion imaging. Typically, there are three acquisition strategies used in 3D advanced diffusion imaging, as illustrated in Figure 9. These depend on the number of measurements N and the b-value(s). The strategies to cover q-space are as follows:

1. Sampling of the whole q-space on a dense 3D Cartesian grid (Figure 9). This sampling scheme is generally associated with diffusion spectrum imaging (DSI).
2. Single-shell spherical sampling (Figure 9) for single b-value in q-space. This sampling scheme is generally called single-shell HARDI. If multiple b-values are used, it is called multishell HARDI.
3. Hybrid sampling schemes use samples that can be along radial lines or other more sophisticated distributions. These schemes are generally called HYDI (HYbrid Diffusion Imaging) (35).

The reader should always keep in mind that the more the measurements acquired, the richer the possibility for

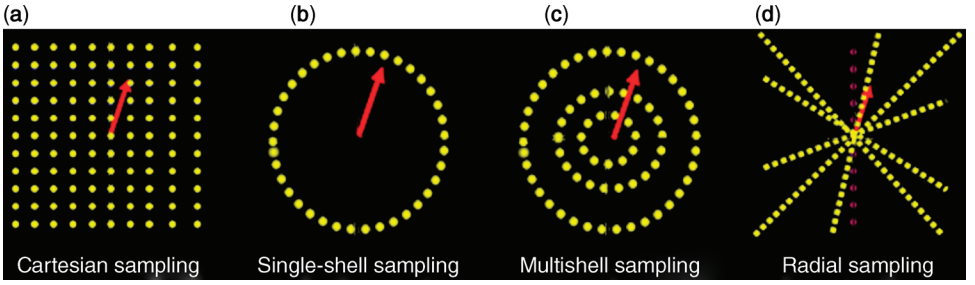

Figure 9. Sampling schemes in q-space. (a) Cartesian sampling dedicated to diffusion spectrum imaging (DSI). (b) Single-shell spherical sampling dedicated to HARDI. (c) Multiple shell and (d) radial sampling schemes dedicated to advanced diffusion propagator imaging and compartment modeling.

reconstruction, but also, as a trade-off, the more the time required to do the HARDI acquisition. Always keep in mind that it takes roughly 10 s to acquire a single diffusion image in a particular gradient direction **g**. Hence, $10N$ is roughly your acquisition time for diffusion MRI. We now review in turn the existing techniques available in the literature. This covers the main ideas and families of techniques published in the last 15 years.

5.2. The Diffusion Signal and Diffusion Propagator

Most of the time, the signal attenuation $E(\mathbf{q}, \boldsymbol{t})$ is considered instead of the signal itself, and corresponds to the diffusion MRI signal $S(\mathbf{q}, \boldsymbol{t})$ normalized by the MRI signal $S(0) = S_0$, $E(\mathbf{q}, t) = S(\mathbf{q}, t)/S_0$, measured in the absence of any diffusion sensitization ($b = 0\,\mathrm{s/mm^2}$). From diffusion MRI, we know that the relation between b, $\mathbf{q}$, and t is $b = t|\mathbf{q}|^2$. Hence, we can mathematically write the diffusion signal in function of b and $\mathbf{g}$, or also from $\mathbf{q}$ and t. It was shown in References 36 and 37 that that there is a Fourier relationship between the signal attenuation $E(\mathbf{q}, t)$ and the diffusion propagator $p(\mathbf{r}, t)$ giving the probability of any displacement $\mathbf{r}$ during the diffusion time t:

$$E(\mathbf{q}, t) = \int_{\mathrm{R}^3} p(\mathbf{r}, t) \exp\left(-2\pi i \mathbf{q}^T \mathbf{r}\right) \mathrm{d}\mathbf{r} \tag{6}$$

Callaghan showed that this relation is true only if the diffusion gradient is infinitely small, or also called the *narrow pulse approximation*. Obtaining diffusion gradient similar to Dirac pulses is impossible on clinical systems, where gradient systems cannot deliver more than 80 mT/m at best, and remains difficult on the connectome gradients (38) that are 300 mT/m or on preclinical systems where the maximum gradient strength does not exceed 1000 mT/m. A direct consequence is that the narrow pulse condition can never be respected. In this case, the position of spin is not instantaneously tagged with a phase driven by the diffusion gradient characteristics, and the tag imposed by a large diffusion gradient set corresponds to an ensemble average position of the spin.

Theoretically, the Fourier relationship of equation 6 imposes to sample the full q-space. This is practically impossible: An infinite magnitude of the $\mathbf{q}$ wave vector would require an infinite gradient strength, and a null magnitude of the wave vector is not possible when considering the existing spatial encoding gradients. In our context and for the purpose of diffusion imaging and HARDI, the most important thing to know is that there is a Fourier transform relationship between the q-space diffusion signal that we measure and the real space probability distribution function that describes the diffusion process of water molecules, also called the *diffusion propagator*. The reader is referred to Reference 39 for more information on the Fourier transform. I often use music as an example to explain the Fourier transform. Each musical note has a certain frequency. For example, A4 has frequency 440 Hz. The Fourier transform of a song can be viewed as the decomposition of the song into the importance of each note (or frequency) in the song. Similarly, the Fourier transform is the tool that allows the MRI machine to "listen" to the water molecules (the hydrogen protons) "sing."

Diffusion Spectrum Imaging. Diffusion spectrum imaging (DSI) is an implementation of q-space imaging in three dimension (36, 37), where a large number of q-space points are taken at every discrete point of the 3D Cartesian grid, most often within a ball defined by the maxima b-value. q-Space is the diffusion frequency space, measured in $\mu\mathrm{m}^{-1}$. From equation 6, the diffusion propagator is then reconstructed using a 3D inverse Fourier transform (F^{-1}) of the normalized measured diffusion MRI signal, $E(\boldsymbol{q}, t)$, on the Cartesian grid (Figure 9):

$$p(\mathbf{r}, t) = F^{-1}(E(\mathbf{q}, t)) \tag{7}$$

The method is partly illustrated in Figure 10. It requires fairly strong imaging gradients ($0 \le b \le 20{,}000\,\mathrm{s/mm^2}$) and a long acquisition time to measure hundreds of diffusion directions and "b-values" (in the range of 150–515 measurements) that cover the 3D Cartesian grid. Maximal b-value needed and q-space Cartesian coverage are still a debate in the community and remain an open question, especially with novel hardware available from the connectome gradients developed for the Human Connectome Project (38). DSI currently remains a research technique that is clinically infeasible because the required acquisition time is too long. There are active developments of new pulse sequences and new undersampling schemes to make DSI possible in less than 20 min (38).

From the diffusion propagator $p(\mathbf{r}, t)$ (eq. 7), one can extract tissue measures such as the mean-squared displacement or return-to-origin probability (34, 40). The mean-squared displacement describes the average

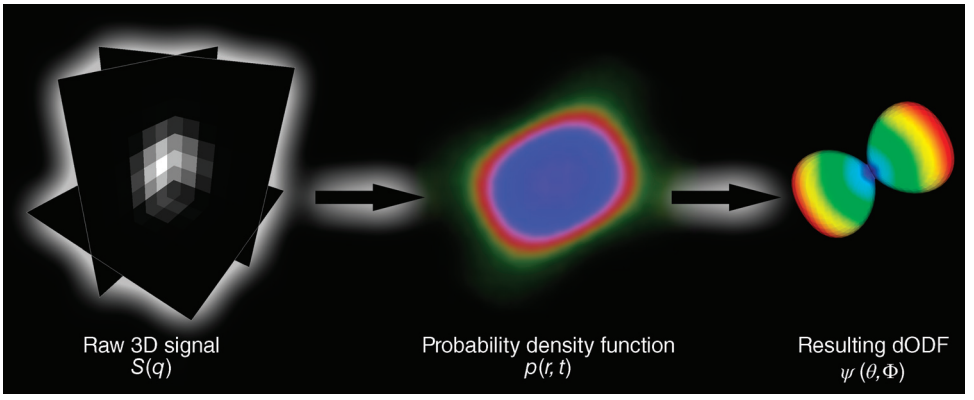

Figure 10. Signal to propagator Fourier relationship and orientation distribution function (ODF). Illustration of the Fourier relationship between 3D diffusion signal $S(\boldsymbol{q}, t)$ and the probability density function, $p(\boldsymbol{r}, t)$, describing the 3D diffusion process of the water molecules. From the diffusion propagator, the diffusion ODF can be computed.

diffusivity within a voxel, whereas the return-to-origin probability describes the probability density of water molecules that minimally diffuse within the diffusion time. These measures still have to make their way into clinical studies but show promising results (35, 41, 42). They show complementary information and richer contrasts than their DTI-based counterpart.

The Orientation Distribution Function (ODF). The most famous feature of the diffusion propagator is the diffusion orientation distribution function, Ψ, capturing the angular content of the diffusion propagator. Recall that the propagator computed from Callaghan's equation 6 does not correspond to the true propagator, but to an ensemble average propagator (EAP). Cory (43) has fortunately demonstrated that this diffusion propagator share the same angular profile as the true propagator, thus enabling the use of the former Fourier relationship to establish models of the local orientation distribution functions of tissues (43). The ODF is thus defined as the radial integral of the diffusion propagator in spherical coordinates:

$$\Psi(\theta, \phi) = \int_0^\infty p(r, \theta, \phi) r^2 \mathrm{d}r \tag{8}$$

where (θ, ϕ) obey physics convention ($\theta \in [0, \pi]$, $\phi \in [0, 2\pi]$). Hence, the diffusion ODF contains the full angular information on the diffusion propagator, as illustrated in Figure 10. It is represented as a spherical function on the unit sphere.

The ODF and its many variants will play a central and crucial role in tractography techniques. Let us take the opportunity to make a small clarification about visualization of ODFs. ODFs can be simple but also complex spherical functions that cannot be visualized as ellipsoids like the diffusion tensors of Figures 5 and 6. The ODF is a discrete function that lives on the sphere. Hence, it can either be represented as a sphere with a certain colormap on it or, as it is most often done, visualized on a spherical mesh where every vertex is scaled by the value of the ODF on the sphere, as illustrated in Figure 11. These are often called glyphs and these glyphs are most often used to visually represent the ODF, but also the diffusion signal on the sphere or any angular function.

The informed reader already has a question in mind: If we are going to reduce the 3D diffusion propagator to a function on the sphere, why measure the whole 3D discrete grid of q-space over hundred of directions in the first place? The answer to this question led to single-shell HARDI

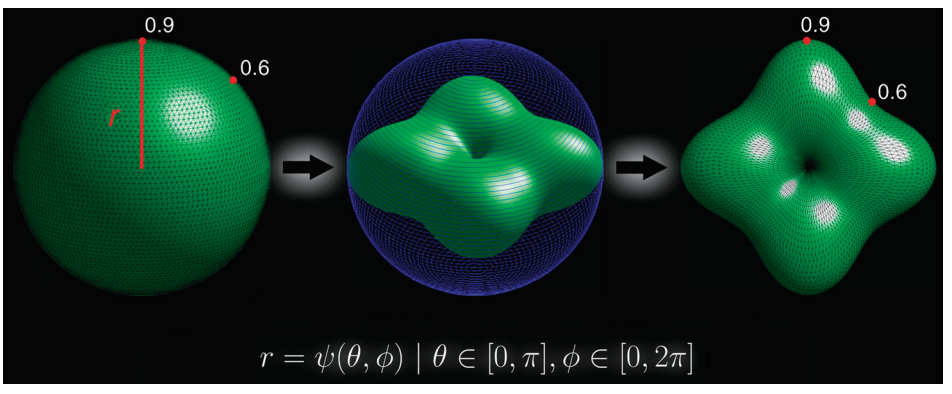

Figure 11. Spherical functions and visualization. A spherical function can be viewed as discrete values that live on the sphere. Hence, one can apply a colormap on a sphere object to visualize it. A more visually appealing option is to scale the radius of each vertex of the sphere according to the value of the sphere. This creates what we call glyphs that can have any shape desired. Hence, these glyphs are used to visualize the diffusion signal, the apparent diffusion coefficient, and the ODF, among other functions, on the sphere.

acquisitions, that is, diffusion measurements for directions acquired for a single b-value, as seen in Figure 9. Single-shell HARDI was the subject of major research developments from the year 2000 until 2010 and remains today an active field of research.

5.3. Single-Shell HARDI

The diffusion signal is measured along gradient directions uniformly distributed on a single shell of q-space, that is, for a single b-value (Figure 9). Most single shell HARDI techniques aim at reconstructing the ODF or variants of this function in order to have an angular function whose maxima are aligned with the underlying fiber structure. Sixty measurements or more and medium gradient strengths are desirable. Typically, $45 \leq N \leq 200$ and $1000 \leq b \leq 4500\,\text{s/mm}^2$ are used and acquisition time is between 5 and 20 min. Therefore, the advantage of single-shell HARDI is that samples are taken only on a single sphere in q-space and, thus, the imaging time is much smaller than that of the DSI despite high angular resolution measurements. Moreover, due to the choice of a smaller b-value, the SNR is greatly improved compared to high b-value images involved in DSI. As of today, in 2014, most HARDI acquisition protocols go for a b-value of $1500\,\text{s/mm}^2$, 60 directions, and 2 mm isotropic resolution for a good signal and angular contrasts.

Given the discrete spherical HARDI measurements, several methods have been proposed to reconstruct estimates of the mixture of fiber compartments, the apparent diffusion coefficient profile, the diffusion ODF, and other diffusion scalar features. More than 100 papers have been published on the subject during 2000–2010. One cannot exhaustively cover all these techniques. In general, methods fall into two categories: model-free and mixture model techniques. Mixture model-based techniques make biophysical assumptions on the fiber populations within an imaging voxel and model how the water molecules diffuse in this assumed environment. On the other hand, model-free techniques do not make physical assumptions about tissue properties. Model-free techniques seek different mathematical representation of the diffusion signal to infer diffusion features.

For educational purposes, we will not follow the historical development of these techniques in time. Model-free techniques will be described first as they highlight properties of the diffusion signal and the diffusion ODF that are crucial to understand HARDI data. Mixture models are then presented. Good reviews can also be found in References 44–46. This is the part of HARDI that is more mathematical and that can be difficult to grasp for the inexperienced reader and user.

Model-Free Techniques. Figure 13 illustrates the fundamental spherical functions and objects involved in single-shell HARDI. First, a discrete spherical grid is required. In practice, a static repulsion algorithm (47) can be used to generate N quasi-uniformly distributed points on the sphere. Alternatively, a geometrical approach can be used, for example, using a specific tessellation order of the icosahedron, producing a specific set of N gradient directions: $\mathbf{g}_i = (\theta_i, \phi_i)$, $1 \leq i \leq N$. These sampling directions define the gradient directions used in the diffusion MRI acquisition. This information is often stored in private tags of the DICOM headers produced by your MRI or not stored at all. DICOM is the image format used by clinical MRI scanners. Hence, it is a good idea to ensure you ask your MR technician to give you the list of gradient directions used by the MRI machine. This information is crucial and mandatory for reconstruction. Depending on your MRI system and options at the console, you can sometimes provide a text file with the gradient directions you want the diffusion MRI sequence to use. Along each of these gradient directions (each vertex in Figure 13), a diffusion signal is measured, $S(\mathbf{g_i})$. Hence, at each imaging voxel, we now have a discrete sampling of the unit sphere along N points: $\mathbf{S} = \{S(\mathbf{g_1}), \ldots, S(\mathbf{g_N})\}$. Therefore, there are two ways to view the diffusion signal. Either as N 3D diffusion images, $S(\mathbf{g_1}), \ldots, S(\mathbf{g_N})$, or as a 4D data set of size X, Y, Z, N.

Mathematics on the Sphere. What is the right mathematical tool to represent $\mathbf{S}$? Many candidates exist, but spherical harmonics (SHs) have made their mark in the HARDI community and were pioneered by References 48 and 49. The spherical harmonics transform is the equivalent of the Fourier transform in the plane but on the sphere. It is thus quite powerful to represent spherical functions. Spherical harmonics of order l and phase m, $Y_l^m, (\theta, \phi)$, arise from the angular solution to Laplace's equation in spherical coordinates and they form an orthonormal basis for complex functions defined on the unit sphere (see Chapter 5 of Reference 29 for a detailed description). Hence, as illustrated in Figure 12, any

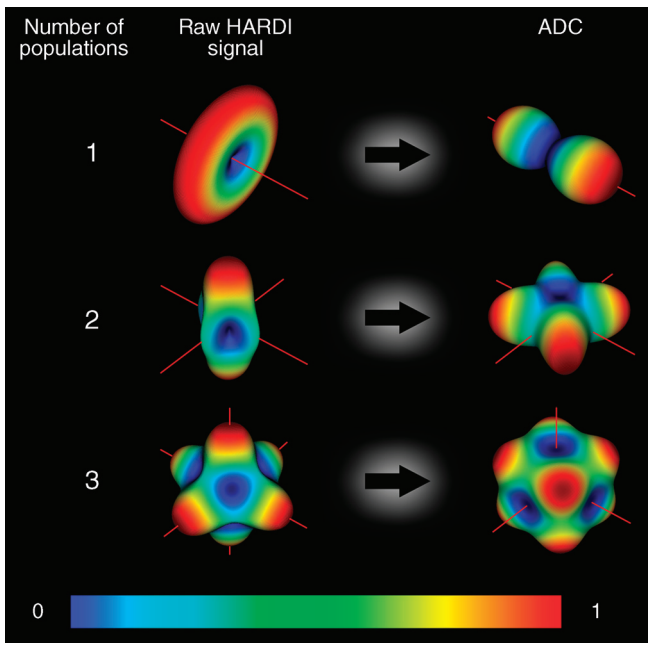

Figure 12. Single-shell HARDI raw signal and apparent diffusion coefficient (ADC). Illustration of the raw diffusion signals and the corresponding ADC profiles for single-, two-, and three-fiber populations. Note how the maximal values of the ADC do not match the underlying directions of the fibers. Hence, the ADC is the wrong object to use for fiber tractography.

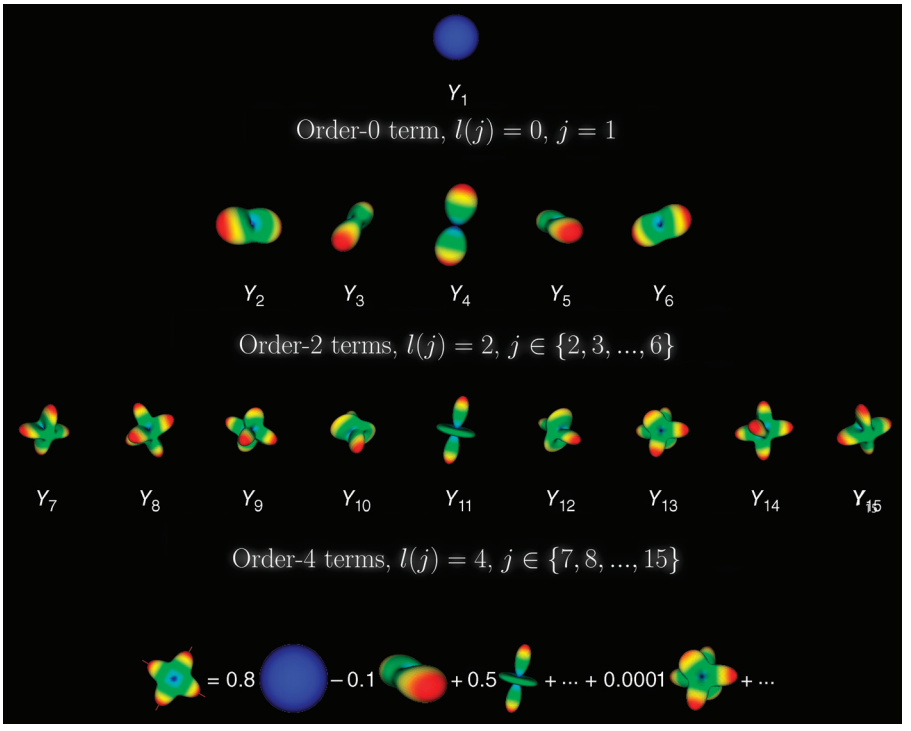

Figure 13. Spherical harmonics basis. Illustration of the first 15 elements of the modified symmetric spherical harmonics basis used to represent diffusion MRI spherical functions on the sphere. The bottom row illustrates that any spherical function can be decomposed as a sum of spherical harmonic coefficients, just like any image can be decomposed as a sum of cosines and sinuses with the Fourier transform. Hence, the spherical harmonics transform on the sphere is equivalent of the Fourier transform in the plane.

spherical function can be decomposed as a sum of spherical harmonic coefficients.

Due to the nature of the diffusion MRI signal, it can be noted that **S** is real and symmetric. Hence, it is common to define a real and symmetric modified orthonormal spherical harmonics basis, Y_j, using only even order terms and real/imaginary parts of $Y_l^m, (\theta, \phi)$ depending on its sign, as illustrated in Figure 12.

Therefore, the measured HARDI signal **S** is estimated with a truncated spherical harmonics series of order $l_{\max}$, which has $R = (l_{\max} + 1)(l_{\max} + 2)/2$ terms. For example, order $l_{\max} = 4$, 6, 8, and 16 SH series have $R = 15$, 28, 45, and 153 coefficients, respectively. The raw HARDI signal is thus estimated as

$$S(\theta, \phi) = \sum_{j=1}^{R} c_j Y_j(\theta, \phi) \tag{9}$$

or in matrix form as $\mathbf{S} = \mathbf{C} \cdot \mathbf{B}$, where $\mathbf{C} = \{c_1, \ . \ . \ . \ , c_R\}$ and $\mathbf{B}$ is the $R \times N$ basis matrix of modified spherical harmonic elements evaluated at each gradient direction, $Y_j(\boldsymbol{g_i})$. Hence, the spherical harmonic coefficients can be obtained with the standard least-squares solutions: $\mathbf{C} = (\mathbf{B}^T\mathbf{B})^{-1}\mathbf{S}$.

Spherical harmonics have other properties that make them very attractive. For instance, many integrals can be solved analytically using the Funk–Hecke theorem (29) and other operators such as the gradient operator or Laplacian operator have analytical expressions (50–52). As a consequence, to deal with noise occurring in high-order frequencies (high-order spherical harmonic coefficients) and better condition for the matrix inversion done in a least-square solution, it has been shown that the best signal estimation with spherical harmonics is done with a small regularization of the coefficients using Tikhonov or Laplace–Beltrami regularization (50, 52, 53). Therefore, the regularized spherical harmonic coefficients are obtained with a linear least-squares solution, including a regularization matrix **L**: $\mathbf{C} = (\mathbf{B}^T\mathbf{B} + \lambda\mathbf{L})^{-1}\mathbf{B}^T\mathbf{S}$. This type of regularization is quite common in computer vision and image processing when solving for large linear systems.

It is important to note that there are other candidates for HARDI representation. High-order diffusion tensors (50, 54, 55) are an alternative representation. They are in fact in a one-to-one relationship with the modified spherical harmonics basis (50, 54), but can offer other powerful properties to extract principal modes of diffusion or invariants (56, 57). More recently, spherical wavelets (58), ridgelets (59), and adaptive kernels using dictionary learning (60) have been introduced. These representations have potential for sparse representations of the diffusion signal. Just as the Fourier transform is not the best representation in the image domain for sparsity (61), other spherical function can be used to have better sparsity properties than spherical harmonics. Combined with a multiresolution wavelet scheme, spherical sparse signal representations are good candidates to represent the diffusion signal with as few coefficients as possible. These novel and more advanced HARDI signal fitting

possibilities become important if one seeks for the HARDI acquisition with the least possible number of directions of the sphere N. These ideas are beyond the scope of this article but are currently very trendy with more and more techniques published to perform compressed-sensing-like reconstructions for HARDI (62). Compressed sensing is a blooming field revolutionizing the concept of the sampling theorem and pushing the limits of undersampled acquisitions. It was pioneered by the seminal papers of Candes (63) and Donoho (64). Compressed sensing can be thought of as a way to by-pass the Fourier transform of equation 7 by an undersampled non-Cartesian pseudo-random acquisition with advanced optimization scheme used for the reconstruction.

With proper mathematical tools to represent the HARDI signal continuously on the sphere, the apparent diffusion coefficient profile, the diffusion ODF, and other features of the diffusion propagator can be extracted more efficiently and robustly.

Apparent Diffusion Coefficient (ADC) Estimation. The first attempts to characterize multiple fiber configurations were made by modeling the apparent diffusion coefficient profile without assuming a single Gaussian diffusion (48, 49), as done in DTI. Recall, as seen with the newspaper example, ADC depends on orientation $\mathrm{ADC}(\theta, \varphi) = \mathrm{ADC}(\mathbf{g})$. Hence, equation 5 is extended to single-shell HARDI and written with respect to the b-value and unit gradient direction $\mathbf{g}$ as

$$S(\mathbf{g}, b) = S_0 \exp(-b \cdot \mathrm{ADC}(\mathbf{g})) \Rightarrow \mathrm{ADC}(\mathbf{g}) = -\frac{1}{b}\ln\left(\frac{S(\mathbf{g}, b)}{S_0}\right) \tag{10}$$

Hence, from N single-shell HARDI measurements, the apparent diffusion coefficient is trivially recovered by taking the natural logarithm of the signal. Then, a spherical harmonics series is used to represent the ADC. As expected, for single-fiber population, the ADC profile resembles the diffusion tensor ellipsoid (Figure 13).

However, even though the ADC reveals information about intravoxel of multiple directions, the maxima of the ADC do not agree with the underlying fiber population, when there are multiple underlying fibers. This was shown *in vivo* in Reference 33 as well as analytically with a cylindrical diffusion model and phantoms (65). This is due to the nature of the ADC, which is the projection of spin displacements onto the diffusing gradient axis. Hence, in the presence of two perpendicular fibers, the greatest diffusion coefficient and greatest signal drop occur at an angle midway between the fibers and not in the direction of either of the fibers, illustrated in Reference 65. Hence, the ADC cannot be used directly to infer the underlying fiber configurations. Nonetheless, the ADC and its compact spherical harmonics representation can be useful to identify the presence of multiple fiber compartments without actually computing the orientations themselves (48–50, 54, 66, 67).

Hence, the next natural question is how to transform the diffusion signal in q-space to a real spherical function aligned with the underlying fiber population, that is, how to go from raw HARDI data to an ODF that we can use to perform fiber tractography.

The Funk–Radon Transform and q-Ball Imaging (qbi). Focusing again on Figure 13, it is striking to see how the diffusion signal is maximal in the plane perpendicular to the underlying fiber population. The Funk–Radon transform (FRT) and q-ball imaging, invented by Tuch (34, 68), exploit this characteristic of the diffusion signal. It computes integrals over great circles defined over the unit sphere, as illustrated in Figure 14. Intuitively, the Funk–Radon transform value at a given spherical point is the great circle integral of the signal on the sphere defined by the plane through the origin perpendicular to the point of evaluation. The Funk–Radon transform is qualitatively illustrated in Figure 14 and performs the desired transformation of the diffusion signal into an ODF aligned with the underlying fiber population. Most importantly, it does so without any *a priori* knowledge on the fiber distribution. The Funk–Radon transform will work for single-fiber population and for 2, 3, and n fiber crossings, as long as there is enough angular resolution.

In fact, Tuch showed that the Funk–Radon transform, which he called q-ball imaging, reconstructs a smoothed version of the true diffusion ODF (eq. 8) directly from a single-shell HARDI acquisition. This q-ball ODF can be obtained analytically from a spherical harmonics estimation of HARDI signal $\mathbf{S}$ (51, 53, 69):

$$\Psi(\theta, \phi) = \sum_{j=1}^{R} 2\pi \frac{c_j}{S_0} P_{l(j)}(0) Y_j(\theta, \phi) \tag{11}$$

where $P_{l(j)}$ is the Legendre polynomial of order l corresponding to the jth coefficient. For $j = 1, 2, 3, 4, 5, 6, 7, \ldots$, $l(j) = 0, 2, 2, 2, 2, 2, 4, \ldots$, respectively. The reader interested in the underlying mathematics and proof for this solution is referred to Reference 29 for all the details.

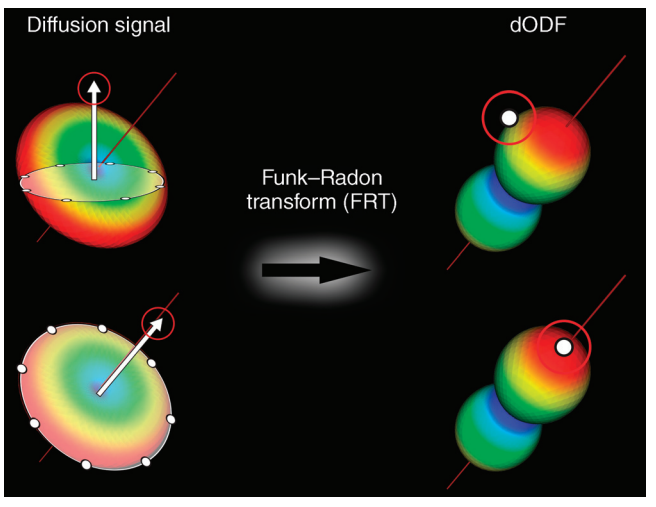

Figure 14. Funk–Radon transform and q-ball imaging. Illustration of the Funk–Radon transform (FRT) that is at the heart of q-ball imaging and ODF reconstruction. Great circle integrals are computed from the measured signal to obtain the ODF.

Comparing equations 9 and 11, we note that the Funk–Radon transform or q-ball imaging is ultimately just a linear transformation of the spherical harmonic coefficients c_j, representing the input HARDI signal $\mathbf{S}$. This technique is called *analytical*-qbi (a-qbi), in contrast to the original q-ball imaging solution, which performs the Funk–Radon transform numerically (68). qbi and a-qbi are available in Dipy (www.dipy.org).

Of course, there are mathematical and practical implications to this simplification of DSI over only a single-shell HARDI. After all, we do not have any radial information in single-shell HARDI and q-ball imaging, as opposed to DSI that has several angular and radial points. In fact, not considering the full radial information of the diffusion signal results in a q-ball ODF that is not intrinsically normalized, that is, the sum of its values on the sphere is not equal to 1. In practice, we ensure the q-ball ODF is normalized numerically. The q-ball ODF in fact computes the following unmarginal radial integral:

$$\Psi(\theta,\phi) = \int_0^\infty p(r,\theta,\phi)\mathrm{d}r \tag{12}$$

Compared to equation 8, the r^2 term is not part of the integral. This normalization issue has led to a "normalized" qbi technique in References 70–73. By adding an assumption on the ADC decay in q-space (exponential decay), one can recover the normalized q-ball ODF, also called the *constant solid angle* (csa)-ODF. The solution remains linear and has a simple spherical harmonic expression. The csa-qbi technique is also available in Dipy (www.dipy.org). The csa-ODF is in close spirit to the diffusion orientation transform (DOT) where the ADC is also assumed to follow an exponential decay or a biexponential or triexponential decay. By inserting this signal modeling decay into the Fourier relationship of equation 7, Reference 74 showed that it is possible to reconstruct the diffusion propagator $p(\mathbf{r}, t)$. It is thus possible to obtain estimates of the propagator at different radii or simply perform the radial integral as in equation 7 to obtain an ODF estimation from the DOT (74).

Anisotropy Measures. Several single-shell HARDI anisotropy measures exist. Just as for DTI, mean diffusivity (MD) is still a candidate, where $\mathrm{MD} = \mathrm{sum}(\mathrm{ADC}(\mathbf{g}))/N$. Otherwise, measures based on the spherical harmonics decomposition or high-order tensor decomposition of the signal or ADC profile have been proposed (48–50, 54, 66, 67). Also, Reference 68 proposed the generalized FA (GFA) as the ratio of the root mean square (rms) to the standard deviation (STD) of the ODF values on the sphere or any other spherical function, that is, $\mathrm{GFA} = \mathrm{STD}(\mathbf{\Psi})/\mathrm{rms}(\mathbf{\Psi})$:

$$\mathrm{GFA} = \sqrt{\frac{N\sum_{i=1}^{N}(\Psi_i - \mathrm{mean}(\mathbf{\Psi}))}{(N-1)\mathrm{sum}(\mathbf{\Psi})}} = \sqrt{1 - f_1^2 / \sum_{j=1}^{R} f_j^2} \tag{13}$$

where $f_j = 2\pi c_i P_{1(j)}(0)$ are the spherical harmonic coefficients of the ODF in equation 11, which simplifies the GFA expression.

Improving Angular Resolution of the Diffusion ODF Reconstruction. Why do we need to improve angular resolution of the diffusion ODF? Here is an intuitive explanation. Diffusion is by nature a "blurry" phenomenon. If one observes ink diffuse on paper, one can quickly see that the process, even if anisotropic, is usually diffusive and blurry. Hence, the diffusion ODF is also, in theory, a blurry object. What does this mean? Suppose we have a 60° crossing between two fiber populations, one fiber population in the Y-direction and the other at Y-60°, as illustrated in Figure 15. The ODF in the (θ, ϕ) orientation tells you what is the probability of having *diffusion* along (θ, ϕ). Hence, the probability of having diffusion in the Y-30° direction is high because it is easy for the water molecules to diffuse in this orientation. Not surprisingly, the corresponding diffusion ODF at Y-30° is actually higher than the value at Y or at Y-60°, as illustrated in Figure 15. This is a problem and an important problem if you think of the fiber tractography application. In a sense, a smoothed diffusion ODF is as limited as a diffusion tensor below a certain degree of crossings (75, 76). This is why the diffusion ODF is not the right object to use for tractography.

A new object is needed for fiber tractography purposes. This object was called the *fiber* ODF (75, 77) or the fiber orientation distribution (FOD) (78, 79). Going back to my previous example, if you now ask what is the fiber ODF value along the (θ, ϕ) orientation at Y-30° direction, the fiber ODF value is very small and in contrary maximal at Y and Y-60° directions. This is illustrated in Figure 15 and is the object one would like to be using for fiber tractography.

Spherical Deconvolution Technique. The reader not familiar with the *convolution* operation must read it first. A classical example of deconvolution is in image

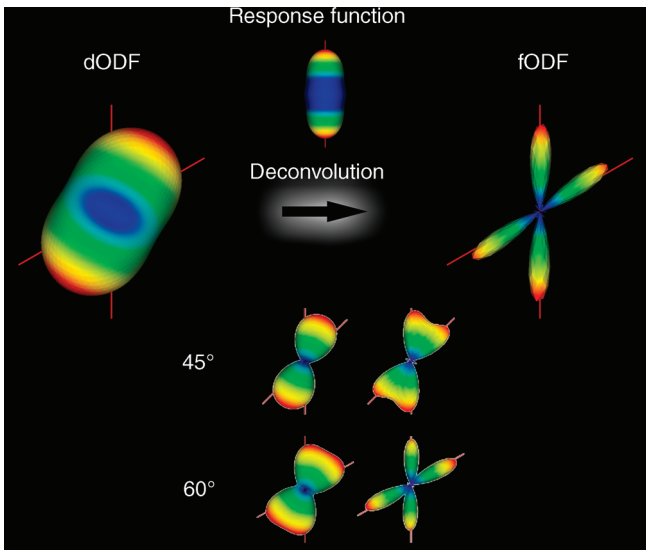

Figure 15. Spherical deconvolution intuition to improve angular resolution of ODF reconstruction. Assuming a particular response function, the deconvolution will remove the "blurry" part of the diffusion ODF to obtain a sharp fiber ODF that better captures the underlying fiber populations. Hence, a better angular resolution can be obtained, as illustrated in 45° and 60° crossing in the bottom of the figure.

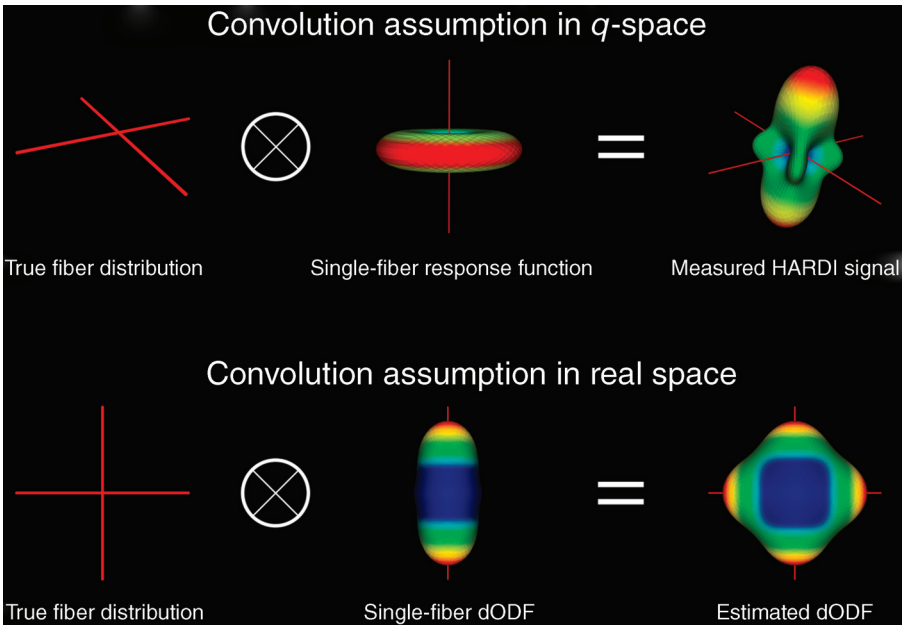

Figure 16. Spherical deconvolution techniques. Convolution assumption in q-space (*signal space*) and real space (*ODF space*). Deconvolution techniques seek to reconstruct the true fiber orientation distribution (FOD) or fiber orientation distribution function (fiber ODF) from an assumed single-fiber response function.

processing. Imagine that you have a perfect high-resolution image with very sharp edges and contrast. Suppose now that you replace every pixel of the image by the average of its neighbors within a certain radius. This creates a blurry image that is the result of a convolution between the original image and the "averaging filter." Thus, deconvolution tries to obtain back the high-resolution original image starting only from the blurred image. If the blurring process is unknown, inverting the convolution operation is known to be an *ill-posed* difficult problem.

Spherical deconvolution (78) was introduced approximately at the same period as q-ball imaging. The original spherical deconvolution method was proposed in Reference 78. Spherical convolution assumes that a distribution of fiber orientations convoluted with a single-fiber response function generates the measured diffusion signal, as illustrated in Figure 16. Hence, the idea is to view the HARDI signal $\mathbf{S}$ as the convolution of the response function produced by a single-fiber $\mathbf{R}$ with the expected true fiber orientation distribution $\mathbf{F}$. This is illustrated in Figure 16. The problem can also be viewed more intuitively in real space using the ODF (Figure 16). The signal or ODF response function used as the deconvolution kernel is normally estimated from the data itself. Typically, we can use the corpus callosum voxels or voxels with a FA above 0.7 to estimate the response function $\mathbf{R}$ there. Alternatively, it can also be directly modeled with an appropriate signal or ODF for a single fiber as done in References 80 and 81. Then, using spherical harmonics theory and the convolution theorem, the problem is defined as a multiplication in spherical harmonics space: $\mathbf{S} = \mathbf{R} \cdot \mathbf{F}$. Hence, using a least-squares formulation, one can solve for the FOD: $\mathbf{F} = (\mathbf{R}^T\mathbf{R})^{-1}\mathbf{S}$. Hence, spherical deconvolution cannot be considered as a model-free technique because it needs a deconvolution kernel. In a sense, it is at the frontiers of model-free and model-based techniques.

However, the linear solution just described of spherical deconvolution suffers from severe instabilities at high harmonic orders (78, 81) that lead to negative fiber ODF values and false spurious peaks. Hence, the original spherical deconvolution method was improved using nonlinear methods to better deal with the instabilities, noise, and negative diffusivities appearing in the deconvolution process (79). It is now established that adding a constrained regularization to ensure positivity and stable deconvolution is crucial to solve the spherical deconvolution inverse problem (52, 69, 75, 79, 81, 82). Note that the Richardson–Lucy approach (80) is intrinsically nonnegatively constrained. Constrained spherical deconvolution is available in MRtrix (83) and Dipy (84). Dipy also has other deconvolution techniques such as the sharpening deconvolution transform (SDT) of Reference 75 and the Lucy–Richardson technique of Reference 80.

The Fiber ODF Amplitude as New Anisotropy Measure. Recently, two groups have separately shown the potential microstructural information contained in the fiber ODF amplitude (85, 86). It is shown how the fiber ODF amplitude is proportional to the underlying fiber density. Hence, Raffelt et al. have defined the new term, *apparent fiber density* (AFD) (85), whereas Dell'Acqua et al. have used the term *hindrance-modulated orientational anisotropy* (HMOA) (86). The term orientational fiber anisotropy might be a good trade-off between the two.

No matter what name is used, it is important to note here that we no longer have a single value per imaging voxel. The AFD or HMOA is a multivalued function that

depends on orientation. This adds complexity when one wants to produce maps for clinical applications. One possibility is to produce maximal or mean maps of fiber amplitudes (86). Or, if used in combination with tractography, one can now follow this measure along the actual tract of interest.

Persistent Angular Structure MRI (PAS-MRI). Finally, another form of ODF is the radially persistent angular structure (PAS) of the diffusion propagator (87). Assuming independence of the angular and radial structures of the diffusion propagator, the formulation forces probabilities to be nonzero only on a spherical shell of radius r. Hence, the PAS is the function on the sphere that best describes the signal measurements and that best represents the relative mobility of spins in each direction. This PAS function is reconstructed by fitting the raw data with a nonlinear iterative algorithm using a maximum entropy cost function. The technique produces ODFs that look sharper than the q-ball and csa-ODF estimation of the diffusion ODF. However, the reconstruction is computationally heavy and can take several hours/days to reconstruct a full brain data set of PAS functions. Recent efforts (88) have been made to propose a linearized solution to PAS-MRI. This is based on the fact that PAS-MRI is a special case of spherical deconvolution methods (81). PAS-MRI is available in Camino (http://cmic.cs.ucl.ac.uk/camino/).

5.4. Compartment Models

As opposed to model-free techniques just described, mixture models make biophysical assumptions about the microstructure of white matter tissue and how water molecules propagate in this environment. Figure 17 illustrates a famous example of a mixture compartment model, where the voxel is separated as the sum of three compartments: one single isotropic compartment serving as a free water part and two single-fiber compartments.

Multi-Gaussian (Tensor) Modeling. Historically, when the community saw that the DTI model failed in fiber crossings, the natural extension was to try more than one tensor per voxel. Hence, in References 33 and 89, it was proposed to model the HARDI signal as a finite mixture

$$S(\mathbf{g}, b) = S_0 \sum_{i=1}^{n} p_i \exp\left(-b\mathbf{g}^T\mathbf{D_i}\mathbf{g}\right) \tag{14}$$

of n tensors with volume fractions p_i to obtain the corresponding diffusion propagator as

$$p(\mathbf{r}, t) = \sum_{i=1}^{n} \frac{p_i}{\sqrt{(4\pi t)^3 |\mathbf{D}_i|}} \exp\left(-\frac{\mathbf{r}^T\mathbf{D}_i^{-1}\mathbf{r}}{4t}\right) \tag{15}$$

Parameters of each Gaussian compartment and volume fractions (p_i) are estimated with an iterative process. The multiple Gaussian modeling also depends on a possibly oversimplified and incorrect fiber model when fixing the number of fiber compartments. However, Reference 90 uses the voxel classification of Reference 49 to automatically select the number of compartments at every voxel. More recent techniques based on the generalization error (91) can also be done. In general, the number of fiber compartments is manually set to $n = 2$. It is however reported that the solution can be quite unstable and considerably affected by the number of measurements and SNR of the diffusion signal. To make the numerical solution more stable, one can make assumptions about the estimated tensors and enforce constraints on the multiple compartments. For example, one can impose symmetry of eigenvalues, force certain magnitude and ratios of eigenvalues, or impose positive definiteness of the DT (33, 34, 90, 92–95), among others. Finally, several more recent multi-tensor extensions have been proposed using diffusion basis function of Gaussians (82) and Kalman filtering (96).

Numerous other mixture models exist using mixtures of spherical functions or directional functions such as Wisharts, Bingham, Watson, von Mises-Fisher, and de la Vallée Poussin functions (97–99). All these mixture models attempt to fit the diffusion signal as best as possible, with as few parameters as possible, to extract measures that can reflect the white matter tissue architecture.

Ball-and-Stick Model. Another important mixture model similar to multi-Gaussian modeling is the *ball-and-stick* mixture model. It assumes that water molecules in an imaging voxel belong to one of two populations, a restricted population within or near fiber structures and a free population that is not affected by fiber structure barriers. Multiple anisotropic Gaussian distributions are used for the restricted population and an isotropic Gaussian distribution is used for the free population. The approach extends to a mixture of restricted compartments and is thus able to recover multiple fiber compartments (100, 101). It may be interesting to report that assuming a simplified model, these compartment models are coming back to a deconvolution model, as stated in Reference 102.

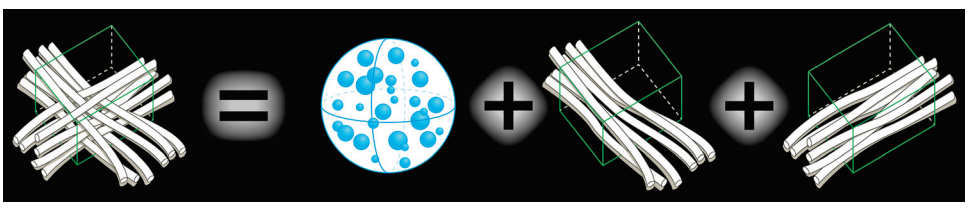

Figure 17. Diffusion compartment models. Example of a mixture compartment model. Here, the imaging voxel is assumed to be composed of a single isotropic compartment and two single-fiber compartments.

Overall, mixture models lead to more complex computational problems, but have the potential to extract *physical parameters* such as volume fraction of fibers in the voxel or isotropic compartment proportion or estimate uncertainty in parameters such as the principal fiber directions. These parameters can be turned into maps and these maps can be used in diffusion MRI applications. Such applications are quickly growing in the literature.

The reader should also keep in mind that these compartment models can always be improved with physically more meaningful models. For instance, it is known that restricted diffusion does not behave like a stick nor does extra-axonal compartment behave like a ball. Nonetheless, this technique is quite popular because it has shown to be robust and has found success in many applications (103, 104). The ball-and-stick model is available in FSL (http://fsl.fmrib.ox.ac.uk/fsl/fslwiki/). For example, a recent extension of the ball-and-stick model is the ball-and-rackets model aiming to model the branching/dispersing behavior of the diffusion signal. This can prove to be important in several locations of the brain (105).

Recently, mixture models have been pushed even further to obtain more than fiber orientations, volume fractions, or free water estimation as parameters. The new *buzzword* is *diffusion microstructure* and *axonal diameter distribution* estimation. These novel and exciting techniques fall under the compartment model family of techniques.

Diffusion Microstructure and 3D Advanced Diffusion Imaging. While most of the developments done in diffusion imaging aimed at inferring the brain connectivity with tractography until the middle of the 2000s, fewer studies were dedicated to the developments of methods able to characterize the microstructure of tissues. Such methods depend on the restriction effect occurring in axons: In the case of free diffusion, the displacement probability is enlarged when the diffusion time increases; in the case of porous media, this enlargement is stopped when the diffusion time is such that a molecule moves to a distance equal to the pore size (keep the tissue paper and newspaper experiment of Figure 2 in mind). Consequently, the diffusion time t is the key parameter providing information about the size of the restricted geometry, as increasing the diffusion time t leads to the water molecule able to explore and bump into the microstructure. These studies were first performed using preclinical systems as their gradient coils can have the required strength (1 T/m) to cover a wide range of diffusion times as the diffusion gradient pulses can be designed to preserve the narrow pulse condition (106, 107).

In 2005, Assaf et al. developed a compartment model of the microstructure of the white matter in order to quantitatively measure the distribution of axon radii (108, 109). This model, called *CHARMED* for Composite Hindered and Restricted ModEl of Diffusion, relies on the decomposition of the white matter into three compartments: an intra-axonal compartment, an intracellular compartment, and an extracellular compartment. The model considers axons as an impermeable and restricted compartment characterized by a non-Gaussian displacement probability, whereas the extracellular and intracellular compartments are considered as hindered compartments characterized by a Gaussian displacement probability:

$$E(\boldsymbol{q},t) = f_{\text{hindered}} E_{\text{hindered}}(\boldsymbol{q},t) + f_{\text{restricted}} E_{\text{restricted}}(\boldsymbol{q},t) \tag{16}$$

This pioneer work launched a new and promising application of diffusion imaging, today known as *diffusion microscopy*. In its original version called *AxCaliber*, the method required lots of samples as not only the q-space had to be sampled but also the diffusion time, preventing it to become usable in clinical application. But in 2008, Alexander et al. developed a simulation framework to tune the acquisition parameters and restrict the number of samples required to infer the distribution of axon radii and volume fractions to a point that makes this method today usable in clinical research. This technique is called *ActiveAx* (110, 111). One needs a multiple b-value and multiple timescale diffusion MRI, which is a topic beyond the scope of this article. It is thus now possible to estimate distributions of mean axonal diameter *in vivo* and these techniques have now opened a new field of research *per se* of diffusion microstructural imaging with novel models and novel optimization techniques being published every month. AxCaliber and the CHARMED model also have clinically feasible prescribed acquisition scheme for 3 Tesla (http://neuroimaging.tau.ac.il/yawiki/index.php/3T_CHARMED). A recent ISMRM diffusion workshop was fully dedicated to this topic and the reader is encouraged to watch the presentations and look at the content (http://www.ismrm.org/workshops/Diffusion13/program.htm). This will be an exciting field of research for the next coming years.

5.5. Beyond Single-Shell HARDI

Since 2005 or so, research groups have thus started bridging the gap between single-shell HARDI and full 3D Cartesian sampling used in DSI. The radial information is brought back into play because, as just mentioned, the radial part of the diffusion signal can be sensitive to microstructural features if the diffusion time is sampled. Hence, more sophisticated modeling such as the CHARMED model (108), AxCaliber (109), ActiveAx (111), diffusion kurtosis imaging (DKI) (112), generalized DTI (55, 113), multitensor models (114), NODDI (115), 3D SHORE (42) among others have appeared to reconstruct intra- and extracellular compartments to estimate axonal diameter distribution and other high-order information.

On the other hand, some works have shown improved ODF angular estimation (35, 41, 73, 116–118) using multiple shell HARDI acquisitions. This is not surprising considering the extra amount of diffusion-weighted images included in the estimation. The ODF estimation thus benefits from the higher SNR of low b-value images and also from the higher angular contrast of the higher b-value images.

Cumulant Expansion and Diffusion Kurtosis Imaging. A last multishell HARDI technique that needs to be mentioned is diffusion kurtosis imaging. Going back to

equation 7, which says that the inverse Fourier transform of the normalized diffusion signal is the diffusion propagator distribution, one can either look at moments of the diffusion propagator or at cumulants of the logarithm of the diffusion signal. Cumulants are very well known in statistics. Taking the natural logarithm of the scalar diffusion signal (eq. 2), we can thus write it as a power series in terms of orders of b-value (112, 113), as

$$\ln(S(b)) = \ln(S_0) - bD_{\text{app}} + \frac{1}{6}b^2 D_{\text{app}}^2 K_{\text{app}} + O\left(b^3\right) \quad (17)$$

where the first-order term in b is D_{app}, the apparent diffusion coefficient of the diffusion tensor seen before in Section 4, and the second-order term in b is the apparent kurtosis K_{app}. This makes it possible to estimate the diffusion kurtosis by taking three diffusion-weighted measurements for three different b-values in addition to the baseline $b = 0$ image S_0. This approach is known as diffusion kurtosis imaging (112). For anisotropic diffusion in three dimension, the diffusion coefficient becomes the diffusion tensor (order 2 Cartesian tensor) and the diffusion kurtosis becomes a fourth-order tensor. The kurtosis tensor is in fact a fourth-order tensor and there are several recent approaches to robustly estimate the kurtosis tensor and measures from it such as the mean apparent kurtosis (119–121). The diffusion kurtosis basically captures the non-Gaussian part of the diffusion signal, that is, K_{app} is high wherever the single-diffusion tensor badly models the signal. This is effective wherever there is more than a single fiber population. Kurtosis has recently gained major interests in applications as an alternative measure that goes beyond DTI measures (122). In a sense, Kurtosis reconstruction is a model-free technique because it is based on the cumulant expansion theorem of the log of the signal and does not assume a particular biophysical model. But, just as DTI is the Gaussian model, DKI can also be seen as a model-based technique based on the second-order statistics. The hypothesis is that a second diffusion tensor in addition to a fourth-order kurtosis tensor can explain the diffusion signal well. However, the cumulant expansion series has a finite radius of convergence centered around $b = 0$ and therefore DKI is useful for intermediate and low b-values $\leq 2500\,\text{s/mm}^2$.

5.6. Summary of q-Space Imaging and HARDI Techniques

A new student in the field by now must have been discouraged with all these reconstruction techniques, models, sampling schemes, and mathematical functions. Do not despair. I have attempted to give an intuitive overview of the field and have given a lot of references and keywords so that you can explore them further. It is normal that you do not grasp every technique described.

One thing to observe is that almost all of the local models come from the Fourier relationship of equation 6 (37). q-Space imaging and HARDI have become fundamental in diffusion imaging, but is still far from being used in clinical routine. The clinic is still at the DTI phase, but as seen here there are numerous richer options possible at the cost of a slightly longer acquisition time. The HARDI community still needs to find the "killer app" for the clinic to justify these longer acquisition times.

Nonetheless, diffusion MRI is a promising tool that may give birth to putative imaging biomarkers characterizing the atrophy of brain diseases at the cellular level in conjunction with the novel diffusion microscopy imaging. The main limitation at the moment is the power of the clinical gradient systems, but hopefully the strength of gradients is improving, thanks to the emergence of ultrahigh-field MRI and the Human Connectome Project.

As seen in this section, there are numerous modeling and estimation techniques possible from HARDI acquisitions. The b-value chosen, the number of shells, and the number of directions will ultimately be governed by the diffusion features that one wants to reconstruct: ODFs, fiber ODFs, apparent density, intra/extra-axonal compartments, free water compartment, dispersion, kurtosis, and others. It is important to note that it remains an open question in the HARDI community to find the best set of acquisition parameters given the object to be reconstructed.

Overall, HARDI estimation can be used for two applications:

1. Local tissue classification studies by extracting diffusion measures. This is possible from the apparent diffusion coefficient, fiber ODFs, and kurtosis analysis, among others. Here, the ultimate quest is to define biomarkers sensitive to white matter tissue anomalies and brain damage.
2. Angular distribution estimation (ODF, fiber ODF, and their variants). This is the first step before robust tractography. From the field of ODF, principal directions are extracted (Figure 18) and white matter bundles can be tracked through regions of

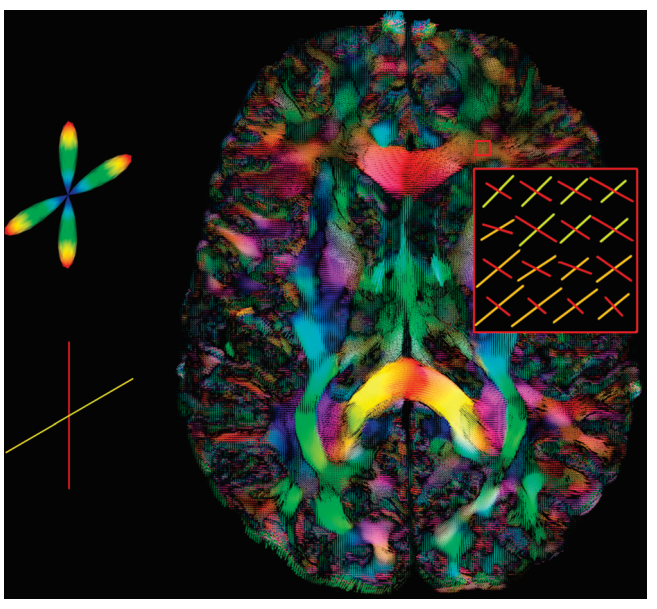

Figure 18. Maxima extraction and HARDI tracking. From fiber ODFs, one can extract the principal directions of the fiber ODF or peaks. Hence, one now has a field of peaks or an image of multiple peaks that can be used for tractography.

Table 3. Recommended Acquisition Parameter *Guide* for Clinical and Research HARDI

Clinical single-shell HARDI	Research single-shell HARDI
$b = 1000\,\text{s/mm}^2$	$b = 1500$–$4500\,\text{s/mm}^2$
$N = 60$ directions	$N \geq 60$ directions
One S_0 image	Two S_0 images every 10 directions in anterior–posterior and posterior–anterior directions to better correct for artefacts
NEX = 1, parallel imaging ON	NEX = 1, parallel imaging ON
2 mm isotropic resolution	1.5 mm isotropic resolution
~15 min (suggestion: divide acquisition into three blocks of 20 directions – 5 min each)	≥30 min

Table 4. Advantages and Limitations of HARDI

Single-shell HARDI advantages	HARDI disadvantages/ limitations
Reasonable acquisition time (~l5 min or less)	Longer acquisition time than DTI (often still too long for the clinic)
Overcomes limitations of DTI in crossing and curving areas	Beyond the local crossing, it cannot differentiate between crossing, kissing, or branching configurations
Robust tractography possible through areas of fibers crossing and curving	HARDI-based measures that reflect tissue property is yet to make a mark in clinical applications

crossing configurations as well as high curvature regions, as illustrated in Figure 18. This overcomes some of the well-known limits of DTI. In practice, if the aimed application is fiber tracking, Table 3 illustrates a typical single-shell HARDI acquisition in clinical or research settings.

5.7. HARDI Limitations

Like DTI, HARDI also has some limitations. HARDI allows recovering crossing configurations if enough angular measurements are given. But which crossing configurations?

Within an imaging voxel, fibers can curve, fan/merge, cross, kiss/bottleneck, or branch/merge and still produce a similar looking ODF. Many different subvoxel configurations can thus lead to the same diffusion ODF and fiber ODF profile (123), as seen in Figure 8. The exact diffusion ODF or FOD that these fiber configurations produce on real data remains unknown and ambiguous. New *ex vivo* phantoms (124–132) and Monte Carlo simulators have started to appear in *Camino* (133), the *numerical* fiber *generator* (134), and phantomas (emmanuelcaruyer.com/phantomas.php) to generate realistic scenes that can mimic these subvoxel configurations and test the local HARDI modeling and estimation techniques. These data sets are crucial for the development and understanding of these subvoxel configuration problems. It is a very local problem that can have global repercussions on tractography results. To our knowledge, only a few research groups have started to address these problems. New tractography methods that can account for fanning configurations in the tracking are being developed, but results are still preliminary, and the more complicated subvoxel configurations are not addressed (105, 123, 135). Others have started to include local geometry information from the neighboring voxels and spatial regularization (136–138).

Nonetheless, HARDI permits the estimation of angular distributions that locally captures multiple fiber crossings and allows for robust tractography. The advantages and limitations of HARDI are summarized in Table 4.

It is now important to explore how to use this local fiber information at every voxel to obtain structural connectivity from fiber tractography techniques.

6. STRUCTURAL CONNECTIVITY FROM HARDI

Diffusion *tractography* or white matter fiber *tracking* is the only noninvasive tool able to obtain information on the structural connectivity *in vivo* of the white matter. Fiber tracking is needed to understand functional coupling between cortical regions of the brain and is important for surgical planning and other medical applications (17, 139, 140). Inferring structural connectivity and its application is a blossoming and ongoing topic in diffusion MRI, which is at the heart of human brain mapping and the novel terms *structural connectome* and *connectomics* (141–143).

Currently, fiber tracking is most commonly implemented using the principal diffusion direction of the diffusion tensor, as illustrated in Figure 6. All imaging systems, even clinical systems, now include a fiber tracking module available for radiologists and medical experts. However, as mentioned several times in this article, an important limitation of the DTI is the Gaussian diffusion assumption, which implies that there can only be a single-fiber population per voxel. At the resolution of DTI acquisitions, this is an important problem since it is known that many voxels have low anisotropy index due to non-Gaussian diffusion coming from multiple fibers crossing, curving, branching, fanning, or in a bottleneck. In fact, fiber tracking algorithms based on the DT follow a large number of false tracts due to tensor profiles that are prolate or can prematurely stop in regions of isotropic tensors. HARDI and advanced diffusion imaging methods have overcome these DTI limitations but that does not mean that the fiber tracking problem is a solved one yet nor less prone to false tracts, as clearly shown by the latest tractography evaluation system *Tractometer* (144). Some fiber bundles such as the superior longitudinal fasciculus (SLF) and cingulum, for example, have been successfully tracked with DTI. However, several recent publications (46, 75, 83, 145) show that fiber bundles are underreconstructed in DTI and can have an important number of invalid connections (144). The fanning of the corticospinal tract to the motor homunculus or the lateral commissural connections of the corpus callosum are great examples where HARDI tracking is superior and DTI tracking is underreconstructed and limited (83).

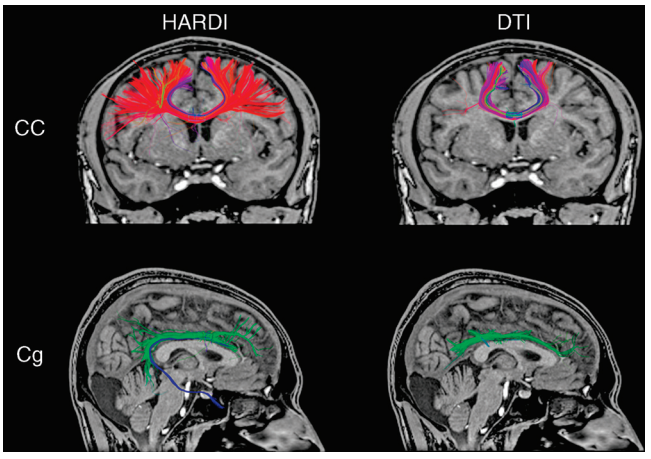

Figure 19. HARDI fiber tracking through crossings versus DTI. Illustration of how HARDI fiber tracking in a field of multiple peaks is superior to DTI fiber tracking based on a field of single peaks from the diffusion tensor. Tracking can traverse complex fiber crossing regions and also better reconstruct high curvature fiber bundles.

Most original DTI-based tractography algorithms have been extended to HARDI-based techniques that better deal with fiber crossings. Fiber tracking is a very intuitive process. The human eye is in fact excellent at fiber tracking, that is, at integrating the possible paths traversing a field of diffusion tensors, ODFs, FODs, or principal directions. What directions to follow? How to follow them? How to numerically perform the computation? These questions are crucial in fiber tracking and depending on how they are answered, four families of algorithms exist: deterministic, probabilistic, geodesic, and global algorithms. Diffusion tractography is a rich topic and deserves a separate article. Good references and introductions can be found in References 5 and 146.

In our context, it is important to point out that nowadays, in 2015, we can overcome the "crossing fiber" problem of DTI with HARDI fiber tracking, as seen in Figure 19. Hence, we obtain much more accurate reconstructions of complex fiber crossing configurations such as the centrum semiovale, but also high curvature and narrower bundles such as the cingulum bundle, the fornix, and many more small "U" fibers than with DTI tractography. It is therefore possible to extract several white matter bundles to perform bundle-specific statistics (147, 148). I sometimes say that tractography can thus serve as a fancy way to obtain more fancy regions-of-interest to perform statistics. Another way to put it is that diffusion tractography is the only noninvasive method to perform white matter *virtual dissection* (149).

6.1. Limitations of HARDI Tractography

In our context, it is also important to point out that we can locally account for crossings. But this does not mean that we know how to follow and how to track through these crossing regions. In fact, this is probably the most important current limitation of HARDI fiber tracking in general. Our local angular reconstructions from HARDI are ambiguous, meaning that several underlying crossing, curving, and branching configurations can lead to the same angular profile (Figure 8). This is a problem for tractography.

Hence, techniques have started looking beyond the voxel to improve tractography and disentangle these local ambiguous crossing configurations. However, this research is very preliminary and one cannot say that HARDI fiber tracking is a solved problem. Optimal choice of tracking method and tracking parameters remains open question (150). A small change in seeding, masking, interpolation, or stopping criteria can have a dramatic impact on fiber tracking output (144). For example, in a neurosurgical planning application, an FA threshold set at 0.15 can produce a tracking result without any fiber passing nearby or projecting into the tumor resection area. However, a slight reduction of this threshold to 0.1, for example, can produce thousands of fiber tracts that cross the resection area of the tumor (140). Better visualization tools that highlight uncertainties in the measurements and in the tracking parameters selection need to be developed for tractography applications.

Moreover, when visualizing and navigating through deterministic, probabilistic, geodesic, and global tracking streamlines, it is striking to see the number of false-positive connections. How do we get rid of these false-positive tracts? Postprocessing commonly filters out some of these false positives by selecting fibers of a particular length or pruning/filtering them with anatomical regions such as deep nuclei or cortical regions. Should postprocessing be used or this pruning should be part of the tracking process itself? Is fiber clustering the way to eliminate false positives? How do we ensure that the tracking reaches the cortex or subcortical regions without the tracking spreading or leaking in gray matter regions? Or do we ensure that a tract really connects to a subcortical region and not just passes nearby or parallel to the structure? These questions are all open and part of active research in the diffusion MRI community. Recent publications such as LIFE (151) and COMMIT (152) have proposed preliminary solutions to address these limitations.

Needless to say, HARDI tractography results come with a large number of skeptical users because of this issue of not controlling false-positive and false-negative tracts, also called *invalid connections* (144). Hence, some experts have a feeling that this tractography technology is still too young to be used (77) and others want to use it right now to answer brain connectivity questions. At the end, the clinical user will have to decide if these tools are useful. As of today, neurosurgeons and neuroradiologists seem to be the most convinced of its importance for neurosurgical planning (140,153, 154).

Nonetheless, several important new HARDI tractography applications are being pushed forward such as structural connectivity mapping (141, 155), connectivity-based parcellation (156–158), and functional/structural connectivity fusion (159–165). All of these applications are very hot topics and most of them are based on a HARDI or 3D advanced diffusion imaging acquisition. In the era of large internationally funded projects in the United States, Europe, China, and elsewhere about mapping the *human connectome* (166), it is safe to say that HARDI tractography, and connectivity research will progress quickly in the coming years.

In summary, as of today, the tractography user needs to be cautious of the limitations of fiber tracking techniques even if HARDI is used and local crossings can be recovered. Care must be taken when interpreting the structural connectivity results before drawing conclusions on brain connectivity and brain function. Looking back at the history of methodological development of diffusion MRI, we can say that it took about 10 years for DTI to appear and overcome limitations of scalar diffusion-weighted imaging (Section 2) and then another 10–15 years to overcome the crossing fiber problem of DTI (Section 3) with HARDI (Section 4). This brings us where we are today, in 2015, where we can envision that it will take the community another 10–20 years to overcome the HARDI tractography limitations.

7. CONCLUSION

This article covered the relatively young history of HARDI: from basic principles of diffusion to diffusion imaging, to diffusion tensor imaging, and to more recent high-angular-resolution diffusion imaging and beyond. From the basic Brownian motion of water molecules, it was seen how one can measure diffusion in one direction and then in three directions to obtain a pseudo-apparent diffusion coefficient. Next, we saw that with a diffusion tensor mathematical framework, a minimum of six measurements was needed to reconstruct the diffusion tensor at every voxel of the brain to extract white matter tissue properties used in clinical diagnostics. DTI is nowadays possible in approximately 3 min on any clinical system. However, the intrinsic limitations of DTI were highlighted in regions of complex fibers crossing and curving. Hence, HARDI and new tractography algorithms were introduced to produce precise full brain tractography. HARDI is nowadays possible on clinical scanners with approximately 5–15 min of acquisition time depending on the parameters chosen. This opens numerous potential applications in neuroscience that require brain connectivity.

The main focus of the article was on HARDI and was presented more with a viewpoint of image reconstruction, analysis, and processing than with a physics viewpoint. Every section of the article detailed the theory and methods necessary and also enumerated the remaining limitations, challenges, and open questions. Among the most important remaining challenges are better spatial, angular, and radial resolution of acquisitions in clinically feasible time, optimal correction of artefacts, optimal local modeling, and local reconstruction techniques and optimal tractography algorithms validated on phantom data and human brain data. Therefore, after reading this article, the new graduate student or diffusion MRI researcher has the big picture of both the state-of-the-art techniques and the limitations and the open problems still to be resolved.

Despite theoretical limitations, acquisition limitations, modeling limitations, tractography limitations, and processing limitations, diffusion MRI and HARDI are great! HARDI is becoming a central part of neuroscience and *connectome* studies. If we are to understand the functioning of the brain, its development and aging, and its diseases, we need to understand how it is wired and connected. Diffusion MRI and HARDI are the non-invasive tool that can bring answers to this challenging quest.

LIST OF ABBREVIATIONS

1D	one-dimensional
3D	three-dimensional
a-qbi	analytical q-ball imaging
ADC	apparent diffusion coefficient
AD	axial diffusivity
CHARMED	composite hindered and restricted model of diffusion
csa-ODF	constant solid angle-orientation distribution function
DKI	diffusion kurtosis imaging
DTI	diffusion tensor imaging
DT	diffusion tensor
DSI	diffusion spectrum imaging
DWI	diffusion-weighted imaging
DW	diffusion-weighted
EAP	ensemble average propagator
FA	fractional anisotropy
FRT	Funk–Radon transform
FOD	fiber orientation distribution
GFA	generalized fractional anisotropy
HARDI	high angular resolution diffusion imaging
MD	mean diffusivity
MRI	magnetic resonance imaging
NEX	number of EXcitations
NMR	nuclear magnetic resonance
ODF	orientation diffusion function
PAS	persistent angular structure
PDF	probability distribution function
PGSE	pulse gradient spin echo
qbi	*q*-ball imaging
qsi	*q*-space imaging
RD	radial diffusivity
RGB	red–green–blue
SD	spherical deconvolution
SH	spherical harmonics
SNR	signal-to-noise ratio

ACKNOWLEDGMENTS

I would like to thank Rachid Deriche, my Ph.D. advisor, and Cyril Poupon, my postdoctoral advisor, for their good training and great insight into diffusion MRI. Large parts of this article were inspired by reports, thesis, papers, and presentations made during my time under their supervision. I would also thank my team, the Sherbrooke Connectivity Imaging Lab (http://scil.dinf.usherbrooke.ca), for their collaboration on this article, especially Johannes Brustle, Samuel St-Jean, and Etienne St-Onge for their help. I would like to especially thanks Alexandre Gauvin for his great artistic work on the figures. Finally, I acknowledge the invaluable input by the reviewer of this article.

BIBLIOGRAPHY

1. R. Brown. A Brief Account of Microscopical Observations Made in the Months of {J}une, {J}uly and {A}ugust, 1827, on the Particles Contained in the Pollen of Plants; and on the General Existence of Active Molecules in Organic and Inorganic Bodies. *Philos. Mag.* **1828**, *4*, pp 161–173.
2. A. Einstein. *Investigations on the Theory of the Brownian Movement*. Dover Publications, 1956.
3. D. LeBihan, R. Turner, and P. Douek. Is Water Diffusion Restricted in Human Brain White Matter? An Echo-Planar NMR Imaging Study. *Neuroreport* **1993**, *4*(7), pp 887–890.
4. H. Johansen-Berg andT. E. J. Behrens, Eds. *Diffusion MRI*. Elsevier, 2009.
5. D. K. Jones. *Diffusion MRI: Theory, Methods, and Applications*. Oxford University Press, 2011.
6. E. O. Stejskal and J. E. Tanner. Spin Diffusion Measurements: Spin Echoes in the Presence of a Time-Dependent Field Gradient. *J. Chem. Phys.* **1965**, *42*, pp 288–292.
7. M. E. Moseley, Y. Cohen, J. Mintorovitch, J. Kucharczyk, J. Tsuruda, P. Weinstein, and D. Norman. Evidence of Anisotropic Self-Diffusion. *Radiology* **1990**, *176*, pp 439–445.
8. P. Douek, R. Turner, J. Pekar, N. J. Patronas, and D. LeBihan. MR Color Mapping of Myelin Fiber Orientation. *J. Comput. Assist. Tomogr.* **1991**, *15*, pp 923–929.
9. P. J. Basser and D. LeBihan. Fiber Orientation Mapping in an Anisotropic Medium with NMR Diffusion Spectroscopy, in *11th Society of Magnetic Resonance in Medicine Meeting*; 1992, p 1221.
10. P. J. Basser, J. Mattiello, and D. LeBihan. Diagonal and Off-Diagonal Components of the Self-Diffusion Tensor: Their Relation to and Estimation from the NMR Spin-Echo Signal, in *11th Society of Magnetic Resonance in Medicine Meeting*; 1992, p 1222.
11. P. J. Basser, J. Mattiello, R. Turner, and D. Le Bihan. Diffusion Tensor Echo-Planar Imaging of Human Brain, in *Proc. of the SMRM*; 1993, p 584.
12. P. J. Basser, J. Mattiello, and D. LeBihan. Estimation of the Effective Self-Diffusion Tensor from the NMR Spin Echo. *J. Magn. Reson. B* **1994**, *103*(3), pp 247–254.
13. P. J. Basser, J. Mattiello, and D. LeBihan. {MR} Diffusion Tensor Spectroscopy and Imaging. *Biophys. J.* **1994**, *66*(1), pp 259–267.
14. C.-F. Westin, S. E. Maier, H. Mamata, A Nabavi, F. A. Jolesz, and R. Kikinis. Processing and Visualization for Diffusion Tensor MRI. *Med. Image Anal.* **2002**, *6*(2), pp 93–108.
15. C. Pierpaoli, P. Jezzard, P. Basser, A. Barnett, and G. D. Chiro. {D}iffusion {T}ensor {MR} Imaging of Human Brain. *Radiology* **1996**, *201*, pp 637–648.
16. G. Kindlmann, D. B. Ennis, R. T. Whitaker, and C.-F. Westin. Diffusion Tensor Analysis with Invariant Gradients and Rotation Tangents. *IEEE Trans. Med. Imaging* **2007**, *26*, pp 1483–1499.
17. S. Mori and P. C. M. van Zijl. Fiber Tracking: Principles and Strategies – A Technical Review. *NMR Biomed*. **2002**, *15*, pp 468–480.
18. J. Neil, J. Miller, P. Mukherjee, and P. S. Huppi. Diffusion Tensor Imaging of Normal and Injured Developing Human Brain: A Technical Review. *NMR Biomed*. **2002**, *15*, pp 543–552.
19. M. A. Horsfield and D. K. Jones. Applications of Diffusion-Weighted and Diffusion Tensor MRI to White Matter Diseases: A Review. *NMR Biomed*. **2002**, *15*, pp 570–577.
20. C. Sotak. The Role of Diffusion Tensor Imaging (DTI) in the Evaluation of Ischemic Brain Injury. *NMR Biomed*. **2002**, *15*, pp 561–569.
21. K. O. Lim and J. A. Helpern. Neuropsychiatric Applications of DTI: A Review. *NMR Biomed*. **2002**, *15*, pp 587–593.
22. J. Sijbers, A. J. den Dekker, M. Verhoye, A. van der Linden, and D. van Dyck. Adaptive Anisotropic Noise Filtering for Magnitude MR Data. *Magn. Reson. Imaging* **1999**, *17*(10), pp 1533–1539.
23. S. Aja-Fernàndez, C. Alberola-Lòpez, and C.-F. Westin. Noise and Signal Estimation in Magniture MRI and Rician Distributed Images: A LMMSE Approach. *IEEE Trans. Image Process.* **2008**, *17*(8), pp 1383–1398.
24. C. G. Koay, E. Özarslan, and P. J. Basser. A Signal Transformational Framework for Breaking the Noise Floor and Its Applications in MRI. *J. Magn. Reson.* **2009**, *197*(2), pp 108–119.
25. P. Coupé, J. V. Manjòon, E. Gedamu, D. Arnold, M. Robles, and D. L. Collins. Robust Rician Noise Estimation for MR Images. *Med. Image Anal.* **2010**, *14*(4), pp 483–493.
26. M. Descoteaux, N. Wiest-Daesslé, S. Prima, C. Barillot, and R. Deriche. Impact of Rician Adapted Non-Local Means Filtering on HARDI. *Med. Image Comput. Comput. Assist. Interv.* **2008**, *11*(Part 2), pp 122–130.
27. C. G. Koay, E. Ozarslan, and P. J. Basser. A Signal Transformational Framework for Breaking the Noise Floor and Its Applications in MRI. *J. Magn. Reson.* **2009**, *197*(2), pp 108–119.
28. P. J. Basser, S. Pajevic, C. Pierpaoli, J. Duda, and A. Aldroubi. *In Vivo* Fiber Tractography Using {DT}-{MRI} Data. *Magn. Reson. Med.* **2000**, *44*, pp 625–632.
29. M. Descoteaux. *High Angular Resolution Diffusion MRI: From Local Estimation to Segmentation and Tractography*. University of Nice-Sophia Antipolis, 2008.
30. B. Jeurissen, A. Leemans, J.-D. Tournier, D. K. Jones, and J. Sijbers. Investigating the Prevalence of Complex Fiber Configurations in White Matter Tissue with Diffusion Magnetic Resonance Imaging. *Hum. Brain Mapp.* **2012**, *34*(11), pp 2747–2766.
31. D. S. Tuch, J. W. Belliveau, T. G. Reese, and V. J. Wedeen. High Angular Resolution Imaging of the Human Brain, in *Proc. of the International Society for the Magnetic Resonance in Medicine*; 1999, p 321.
32. V. J. Wedeen, T. G. Reese, D. S. Tuch, M. R. Wiegel, J.-G. Dou, R. M. Weiskoff, and D. Chessler. Mapping Fiber Orientation Spectra in Cerebral White Matter with Fourier-Transform Diffusion MRI, in *Proc. of the International Society of Magnetic Resonance in Medicine*; 2000, p 82.
33. D. S. Tuch, T. G. Reese, M. R. Wiegell, N. G. Makris, J. W. Belliveau, and V. J. Wedeen. High Angular Resolution Diffusion Imaging Reveals Intravoxel White Matter Fiber Heterogeneity. *Magn. Reson. Med.* **2002**, *48*(4), pp 577–582.
34. D. S. Tuch. *Diffusion MRI of Complex Tissue Structure*. Harvard University and Massachusetts Institute of Technology, 2002.
35. Y.-C. Wu and A. L. Alexander. Hybrid Diffusion Imaging. *Neuroimage* **2007**, *36*, pp 617–629.
36. P. T. Callaghan, C. D. Eccles, and Y. Xia. Rapid Communication: NMR Microscopy of Dynamic Displacements: k-Space and q-Space Imaging. *J. Phys. E* **1988**, *21*, pp 820–822.
37. P. T. Callaghan. *Principles of Nuclear Magnetic Resonance Microscopy*. Oxford University Press: Oxford, 1991.

38. K. Setsompop, R. Kimmlingen, E. Eberlein, T. Witzel, J. Cohen-Adad, J. A. McNab, B. Keil, M. D. Tisdall, P. Hoecht, P. Dietz, S. F. Cauley, V. Tountcheva, V. Matschl, V. H. Lenz, K. Heberlein, A. Potthast, H. Thein, J. Van Horn, A. Toga, F. Schmitt, and E. Al. Pushing the Limits of *In Vivo* Diffusion MRI for the Human Connectome Project. *Neuroimage* **2013**, *80*, pp 220–233.
39. R. N. Bracewell. *The Fourier Transform and Its Applications*. McGraw-Hill Higher Education, 2000; p 616.
40. V. J. Wedeen, P. Hagmann, W.-Y. I. Tseng, T. G. Reese, and R. M. Weisskoff. Mapping Complex Tissue Architecture with Diffusion Spectrum Magnetic Resonance Imaging. *Magn. Reson. Med.* **2005**, *54*(6), pp 1377–1386.
41. M. Descoteaux, R. Deriche, D. Le Bihan, J.-F. Mangin, and C. Poupon. Multiple q-Shell Diffusion Propagator Imaging. *Med. Image Anal.* **2011**, *15*(4), pp 603–621.
42. E. Ozarslan, C. G. Koay, T. M. Shepherd, M. E. Komlosh, M. O. Irfanoğlu, C. Pierpaoli, and P. J. Basser. Mean Apparent Propagator (MAP) MRI: A Novel Diffusion Imaging Method for Mapping Tissue Microstructure. *Neuroimage* **2013**, *78*, pp 16–32.
43. D. G. Cory. Measurement of Translational Displacement Probabilities by NMR: An Indicator of Compartmentation. *Magn. Reson. Med.* **1990**, *14*(3), pp 435–444.
44. P. Hagmann, L. Jonasson, P. Maeder, J.-P. Thiran, V. J. Wedeen, and R. Meuli. Understanding Diffusion MR Imaging Techniques: From Scalar Diffusion-Weighted Imaging to Diffusion Tensor Imaging and Beyond. *RadioGraphics* **2006**, *26*, pp S205–S223.
45. S. Seunarine, K. and D. C. Alexander. Multiple Fibres: Beyond the Diffusion Tensor. In *Diffusion MRI;* Behrens, T. E.; Johansen-Berg, H., Eds.;Elsevier, 2009; pp 55–72.
46. J.-D. Tournier, S. Mori, and A. Leemans. Diffusion Tensor Imaging and Beyond. *Magn. Reson. Med.* **2011**, *65*(6), pp 1532–1556.
47. D. K. Jones, M. A. Horsfield, and A. Simmons. Optimal Strategies for Measuring Diffusion in Anisotropic Systems by Magnetic Resonance Imaging. *Magn. Reson. Med.* **1999**, *42*, pp 515–525.
48. L. R. Frank. Characterization of Anisotropy in High Angular Resolution Diffusion-Weighted {MRI}. *Magn. Reson. Med.* **2002**, *47*(6), pp 1083–1099.
49. D. C. Alexander, G. J. Barker, and S. R. Arridge. Detection and Modeling of Non-Gaussian Apparent Diffusion Coefficient Profiles in Human Brain Data. *Magn. Reson. Med.* **2002**, *48*, pp 331–340.
50. M. Descoteaux, E. Angelino, S. Fitzgibbons, and R. Deriche. Apparent Diffusion Coefficients from High Angular Resolution Diffusion Imaging: Estimation and Applications. *Magn. Reson. Med.* **2006**, *56*(2), pp 395–410.
51. M. Descoteaux, E. Angelino, S. Fitzgibbons, and R. Deriche. Regularized, Fast, and Robust Analytical q-Ball Imaging. *Magn. Reson. Med.* **2007**, *58*(3), pp 497–510.
52. K. E. Sakaie and M. J. Lowe. An Objective Method for Regularization of Fiber Orientation Distributions Derived from Diffusion-Weighted MRI. *Neuroimage* **2007**, *34*, pp 169–176.
53. C. P. Hess, P. Mukherjee, E. T. Han, D. Xu, and D. B. Vigneron. q-Ball Reconstruction of Multimodal Fiber Orientations Using the Spherical Harmonic Basis. *Magn. Reson. Med.* **2006**, *56*, pp 104–117.
54. E. Özarslan and T. H. Mareci. Generalized Diffusion Tensor Imaging and Analytical Relationships between Diffusion Tensor Imaging and High Angular Resolution Imaging. *Magn. Reson. Med.* **2003**, *50*, pp 955–965.
55. C. Liu, R. Bammer, B. Acar, and M. E. Moseley. Characterizing Non-Gaussian Diffusion by Using Generalized Diffusion Tensors. *Magn. Reson. Med.* **2004**, *51*, pp 924–937.
56. A. Ghosh, D. Wassermann, and R. Deriche. A Polynomial Approach for Maxima Extraction and Its Application to Tractography in HARDI. *Inf. Process. Med. Imaging* **2011**, *22*, pp 723–734.
57. A. Ghosh, T. Papadopoulo, and R. Deriche. Biomarkers for HARDI: 2nd & 4th Order Tensor Invariants, in *9th IEEE International Symposium on Biomedical Imaging (ISBI)*; 2012, pp 26–29.
58. I. Kezele, M. Descoteaux, C. Poupon, F. Poupon, and J.-F. Mangin. Spherical Wavelet Transform for ODF Sharpening. *Med. Image Anal.* **2010**, *14*(3), pp 332–342.
59. O. V Michailovich and Y. Rathi. On Approximation of Orientation Distributions by Means of Spherical Ridgelets. *IEEE Trans. Image Process.* **2009**, *19*(2), pp 461–477.
60. S. Merlet, E. Caruyer, A. Ghosh, and R. Deriche. A Computational Diffusion MRI and Parametric Dictionary Learning Framework for Modeling the Diffusion Signal and Its Features. *Med. Image Anal.* **2013**, *17*(7), pp 830–843.
61. D. S. Mallat. *A Wavelet Tour of Signal Processing*. Academic Press, 1999.
62. A. Daducci, E. Canales-Rodriguez, M. Descoteaux, Y. Gur, M. Mani, S. Merlet, A. Ramirez-Manzanares, P. Rodrigues, M. Reisert, and F. Sepehrband. Quantitative Comparison of Reconstruction Methods for Intra-Voxel Fiber Recovery from Diffusion MRI. *IEEE Trans. Med. Imaging* **2013**, *33*(2), pp 384–399.
63. E. J. Candes. Compressive Sampling, in *Proc. of the International Congress of Mathematicians*; 2006.
64. D. L. Donoho. Compressed Sensing. *IEEE Trans Inf. Theory* **2006**, *52*(4), pp 1289–1306.
65. E. A. von dem Hagen and R. M. Henkelman. Orientational Diffusion Reflects Fiber Structure within a Voxel. *Magn. Reson. Med.* **2002**, *48*, pp 454–459.
66. Y. Chen, W. Guo, Q. Zeng, X. Yan, F. Huang, H. Zhang, G. He, B. C. Vemuri, and Y. Liu. Estimation, Smoothing, and Characterization of Apparent Diffusion Coefficient Profiles from High Angular Resolution DWI. *Comput. Vis. Pattern Recognit.* **2004**, *1*, pp 588–593.
67. V. Prckovska, A. Vilanova, C. Poupon, B. ter Haar Romeny, and M. Descoteaux. Classification of Non-Gaussian Diffusion Profiles for HARDI Data Simplification, in *Proc. of the International Society for Magnetic Resonance in Medicine*; 2010.
68. D. Tuch. q-Ball Imaging. *Magn. Reson. Med.* **2004**, *52*(6), pp 1358–1372.
69. A. W. Anderson. Measurements of Fiber Orientation Distributions Using High Angular Resolution Diffusion Imaging. *Magn. Reson. Med.* **2005**, *54*, pp 1194–1206.
70. A. Barnett. Theory of q-ball Imaging Redux: Implications for Fiber Tracking. *Magn. Reson. Med.* **2009**, *62*(4), pp 910–923.
71. E. J. Canales-Rodr'iguez, L. Melie-Garc'ia, and Y. Iturria-Medina. Mathematical Description of q-Space in Spherical Coordinates: Exact q-Ball Imaging. *Magn. Reson. Med.* **2009**, *61*(6), pp 1350–1367.
72. A. Tristán-Vega, C.-F. Westin, and S. Aja-Fernández. A New Methodology for the Estimation of Fiber Populations in the White Matter of the Brain with the Funk–Radon Transform. *Neuroimage* **2010**, *49*(2), pp 1301–1315.

73. I. Aganj, C. Lenglet, G. Sapiro, E. Yacoub, K. Ugurbil, and N. Harel. Reconstruction of the Orientation Distribution Function in Single- and Multiple-Shell q-Ball Imaging within Constant Solid Angle. *Magn. Reson. Med.* **2010**, *64*(2), pp 554–566.
74. E. Özarslan, T. M. Shepherd, B. C. Vemuri, S. J. Blackband, and T. H. Mareci. Resolution of Complex Tissue Microarchitecture Using the Diffusion Orientation Transform (DOT). *Neuroimage* **2006**, *31*(3), pp 1086–1103.
75. M. Descoteaux, R. Deriche, T. R. Knösche, and A. Anwander. Deterministic and Probabilistic Tractography Based on Complex Fibre Orientation Distributions. *IEEE Trans. Med. Imaging* **2009**, *28*(2), pp 269–286.
76. M. Catani, I. Bodi, and F. Dell'Acqua. Comment on "The Geometric Structure of the Brain Fiber Pathways." *Science* **2012**, *337*(6102), p 1605.
77. D. K. Jones, T. R. Knösche, and R. Turner. White Matter Integrity, Fiber Count, and Other Fallacies: The Do's and Don'ts of Diffusion MRI. *Neuroimage* **2013**, *73*, pp 239–254.
78. J.-D. Tournier, F. Calamante, D. G. Gadian, and A. Connelly. Direct Estimation of the Fiber Orientation Density Function from Diffusion-Weighted MRI Data Using Spherical Deconvolution. *Neuroimage* **2004**, *23*, pp 1176–1185.
79. J.-D. Tournier, F. Calamante, and A. Connelly. Robust Determination of the Fibre Orientation Distribution in Diffusion MRI: Non-Negativity Constrained Super-Resolved Spherical Deconvolution. *Neuroimage* **2007**, *35*(4), pp 1459–1472.
80. F. Dell'Acqua, G. Rizzo, P. Scifo, R. A. Clarke, G. Scotti, and F. Fazio. A Model-Based Deconvolution Approach to Solve Fiber Crossing in Diffusion-Weighted MR Imaging. *IEEE Trans. Biomed. Eng.* **2007**, *54*(3), pp 462–472.
81. D. C. Alexander. Maximum Entropy Spherical Deconvolution for Diffusion MRI, in *Image Processing in Medical Imaging*; 2005, pp 76–87.
82. A. Ramirez-Manzanares, M. Rivera, B. C. Vemuri, P. Carney, and T. Mareci. Diffusion Basis Functions Decomposition for Estimating White Matter Intravoxel Fiber Geometry. *IEEE Trans. Med. Imaging* **2007**, *26*(8), pp 1091–1102.
83. J.-D. Tournier, F. Calamante, and A. Connelly. MRtrix: Diffusion Tractography in Crossing Fiber Regions. *Int. J. Imaging Syst. Technol.* **2012**, *22*(1), pp 53–66.
84. E. Garyfallidis, M. Brett, B. Amirbekian, A. Rokem, S. van der Walt, M. Descoteaux, and I. Nimmo-Smith. Dipy, A Library for the Analysis of Diffusion MRI Data. *Front. Neuroinform.* **2014**, *8*, p 8.
85. D. Raffelt, J.-D. Tournier, S. Rose, G. R. Ridgway, R. Henderson, S. Crozier, O. Salvado, and A. Connelly. Apparent Fibre Density: A Novel Measure for the Analysis of Diffusion-Weighted Magnetic Resonance Images. *Neuroimage* **2012**, *59*(4), pp 3976–3994.
86. F. Dell'acqua, A. Simmons, S. C. R. Williams, and M. Catani. Can Spherical Deconvolution Provide More Information Than Fiber Orientations? Hindrance Modulated Orientational Anisotropy, A True-Tract Specific Index to Characterize White Matter Diffusion. *Hum. Brain Mapp.* **2012**, *34*(10), pp 2464–2483.
87. K. M. Jansons and D. C. Alexander. Persistent Angular Structure: New Insights fom Diffusion Magnetic Resonance Imaging Data. *Inverse Probl*. **2003**, *19*, pp 1031–1046.
88. K. K. Seunarine and D. C. Alexander. Linear Persistent Angular Structure MRI and Non-Linear Spherical Deconvolution for Diffusion MRI, in *International Society for Magnetic Resonance in Medicine*; 2006, p 2726.
89. B. A. Inglis, E. L. Bossart, D. L. Buckley, E. D. W. III, and T. H. Mareci. Visualization of Neural Tissue Water Compartments Using Biexponential Diffusion Tensor MRI. *Magn. Reson. Med.* **2001**, *45*, pp 580–587.
90. R. Blyth, P. Cook, and D. C. Alexander. Tractography with Multiple Fibre Directions, in *Proc. of the International Society of Magnetic Resonance in Medicine*; 2003, p 240.
91. B. Scherrer, M. Taquet, and S. K. Warfield. Reliable Selection of the Number of Fascicles in Diffusion Images by Estimation of the Generalization Error. *Inf. Process. Med. Imaging* **2013**, *23*, pp 742–753.
92. K. M. Hasan, P. J. Basser, D. L. Parker, and A. L. Alexander. Analytical Computation of the Eigenvalues and Eigenvectors in {DT}-{MRI}. *J. Magn. Reson.* **2001**, *152*(1), pp 41–47.
93. Y. Chen, W. Guo, Q. Zeng, G. He, B. C. Vemuri, and Y. Liu. Recovery of Intra-Voxel Structure from HARD DWI, in *International Symposium on Biomedical Imaging*; 2004, pp 1028–1031.
94. S. E. Maier, S. Vajapeyam, H. Mamata, C.-F. Westin, F. A. Jolesz, and R. V Mulkern. Biexponential Diffusion Tensor Analysis of Human Brain Diffusion Data. *Magn. Reson. Med.* **2004**, *51*, pp 321–330.
95. S. Peleda, O. Friman, F. Jolesz, and C.-F. Westin. Geometrically Constrained Two-Tensor Model for Crossing Tracts in DWI. *Magn. Reson. Imaging* **2006**, *24*, pp 1263–1270.
96. J. G. Malcolm, M. E. Shenton, and Y. Rathi. Filtered Multitensor Tractography. *IEEE Trans. Med. Imaging* **2010**, *29*(9), pp 1664–1675.
97. T. McGraw, B. C. Vemuri, B. Yezierski, and T. Mareci. Von Mises–Fisher Mixture Model of the Diffusion ODF, in *3rd IEEE International Symposium on Biomedical Imaging (ISBI): Macro to Nano*; 2006.
98. B. Jian, B. C. Vemuri, E. Ozarslan, P. R. Carney, and T. H. Mareci. A Novel Tensor Distribution Model for the Diffusion-Weighted MR Signal. *Neuroimage* **2007**, *37*, pp 164–176.
99. Y. Rathi, O. Michailovich, M. E. Shenton, and S. Bouix. Directional Functions for Orientation Distribution Estimation. *Med. Image Anal.* **2009**, *13*(3), pp 432–444.
100. T. Hosey, G. Williams, and R. Ansorge. Inference of Multiple Fiber Orientation in High Angular Resolution Diffusion Imaging. *Magn. Reson. Med.* **2005**, *54*, pp 1480–1489.
101. T. E. J. Behrens, H. Johansen-Berg, S. Jbabdi, M. F. S. Rushworth, and M. W. Woolrich. Probabilistic Diffusion Tractography with Multiple Fibre Orientations: What Can We Gain? *Neuroimage* **2007**, *34*(1), pp 144–155.
102. T. E. J. Behrens, M. W. Woolrich, M. Jenkinson, H. Johansen-Berg, R. G. Nunes, S. Clare, P. M. Matthews, J. M. Brady, and S. M. Smith. Characterization and Propagation of Uncertainty in Diffusion-Weighted MR Imaging. *Magn. Reson. Med.* **2003**, *50*, pp 1077–1088.
103. T. E. J. Behrens, H. Johansen-Berg, M. W. Woolrich, S. M. Smith, C. A. M. Wheeler-Kingshott, P. A. Boulby, G. J. Barker, E. L. Sillery, K. Sheehan, O. Ciccarelli, A. J. Thompson, J. M. Brady, and P. M. Matthews. Non-Invasive Mapping of Connections between Human Thalamus and Cortex Using Diffusion Imaging. *Nat. Neurosci.* **2003**, *6*(7), pp 750–757.
104. S. Jbabdi and H. Johansen-Berg. Tractography: Where Do We Go from Here? *Brain Connect*. **2011**, *1*(3), pp 169–183.
105. S. N. Sotiropoulos, T. E. J. Behrens, and S. Jbabdi. Ball and Rackets: Inferring Fiber Fanning from Diffusion-Weighted MRI. *Neuroimage* **2012**, *60*(2), pp 1412–1425.

106. Y. Assaf, A. Mayk, and Y. Cohen. Displacement Imaging of Spinal Cord Using *q*-Space Diffusion-Weighted MRI. *Magn. Reson. Med.* **2000**, *44*, pp 713–722.

107. Y. Cohen and Y. Assaf. High *b*-Value *q*-Space Analyzed Diffusion-Weighted MRS and MRI in Neuronal Tissues: A Technical Review. *NMR Biomed*. **2002**, *15*, pp 516–542.

108. Y. Assaf and P. J. Basser. Composite Hindered and Restricted Model of Diffusion (CHARMED) MR Imaging of the Human Brain. *Neuroimage* **2005**, *27*(1), pp 48–58.

109. Y. Assaf, T. Blumenfeld-Katzir, Y. Yovel, and P. J. Basser. AxCaliber: A Method for Measuring Axon Diameter Distribution from Diffusion MRI. *Magn. Reson. Med.* **2008**, *59*(6), pp 1347–1354.

110. D. C. Alexander. A General Framework for Experiment Design in Diffusion MRI and Its Application in Measuring Direct Tissue-Microstructure Features. *Magn. Reson. Med.* **2008**, *60*(2), pp 439–448.

111. D. C. Alexander, P. L. Hubbard, M. G. Hall, E. A. Moore, M. Ptito, G. J. M. Parker, and T. B. Dyrby. Orientationally Invariant Indices of Axon Diameter and Density from Diffusion MRI. *Neuroimage* **2010**, *52*(4), pp 1374–1389.

112. J. H. Jensen, J. A. Helpern, A. Ramani, H. Lu, and K. Kaczynski. Diffusional Kurtosis Imaging: The Quantification of Non- Gaussian Water Diffusion by Means of Magnetic Resonance Imaging. *Magn. Reson. Med.* **2005**, *53*, pp 1432–1440.

113. C. Liu, S. C. Mang, and M. E. Moseley. *In Vivo* Generalized Diffusion Tensor Imaging (GDTI) Using Higher-Order Tensors (HOT). *Magn. Reson. Med.* **2010**, *63*(1), pp 243–252.

114. B. Scherrer and S. K. Warfield. Why Multiple *b*-Values Are Required for Multi-Tensor Models: Evaluation with a Constrained Log-Euclidean Model, in *2010 IEEE International Symposium on Biomedical Imaging: From Nano to Macro*; 2010, pp 1389–1392.

115. H. Zhang, T. Schneider, C. A. Wheeler-Kingshott, and D. C. Alexander. NODDI: Practical *In Vivo* Neurite Orientation Dispersion and Density Imaging of the Human Brain. *Neuroimage* **2012**, *61*(4), pp 1000–1016.

116. M. H. Khachaturian, J. J. Wisco, and D. S. Tuch. Boosting the Sampling Efficiency of *q*-Ball Imaging Using Multiple Wavevector Fusion. *Magn. Reson. Med.* **2007**, *57*, pp 289–296.

117. Y.-C. Wu, A. S. Field, and A. L. Alexander. Computation of Diffusion Function Measures in *q*-Space Using Magnetic Resonance Hybrid Diffusion Imaging. *IEEE Trans. Med. Imaging* **2008**, *27*(6), pp 858–865.

118. H.-E. Assemlal, D. Tschumperlé, and L. Brun. Efficient and Robust Computation of PDF Features from Diffusion MR Signal. *Med. Image Anal.* **2009**, *13*(5), pp 715–729.

119. A. Tabesh, J. H. Jensen, B. A. Ardekani, and J. A. Helpern. Estimation of Tensors and Tensor-Derived Measures in Diffusional Kurtosis Imaging. *Magn. Reson. Med.* **2011**, *65*(3), pp 823–836.

120. A. Ghosh, T. Milne, and R. Deriche. Constrained Diffusion Kurtosis Imaging Using Ternary Quartics & MLE. *Magn. Reson. Med.* **2013**, *71*(4), pp1581–1591.

121. J. Veraart, W. Van Hecke, and J. Sijbers. Constrained Maximum Likelihood Estimation of the Diffusion Kurtosis Tensor Using a Rician Noise Model. *Magn. Reson. Med.*, **2011**, *66*(3), pp 678–686.

122. A. Tabesh, J. H. Jensen, B. A. Ardekani, and J. A. Helpern. Estimation of Tensors and Tensor-Derived Measures in Diffusional Kurtosis Imaging. *Magn. Reson. Med.* **2011**, *65*(3), pp 823–836.

123. P. Savadjiev, J. S. W. Campbell, M. Descoteaux, R. Deriche, G. B. Pike, and K. Siddiqi. Labeling of Ambiguous Subvoxel Fibre Bundle Configurations in High Angular Resolution Diffusion MRI. *Neuroimage* **2008**, *41*(1), pp 58–68.

124. C. P. Lin, V. J. Wedeen, J. H. Chen, C. Yao, and W. Y. I. Tseng. Validation of Diffusion Spectrum Magnetic Resonance Imaging with Manganese-Enhanced Rat Optic Tracts and *Ex Vivo* Phantoms. *Neuroimage* **2003**, *19*, pp 482–495.

125. M. Perrin, C. Poupon, Y. Cointepas, B. Rieul, N. Golestani, C. Pallier, D. Riviere, A. Constantinesco, D. Le Bihan, and J.-F. Mangin. Fiber Tracking in *q*-Ball Fields Using Regularized Particle Trajectories, in *Information Processing in Medical Imaging*; 2005, pp 52–63.

126. J. S. W. Campbell, P. Savadjiev, K. Siddiqi, and G. B. Pike. Validation and Regularization in Diffusion MRI Tractography, in *Third IEEE International Symposium on Biomedical Imaging (ISBI): From Nano to Macro*; 2006, pp 351–354.

127. C. Poupon, B. Rieul, I. Kezele, M. Perrin, F. Poupon, and J.-F. Mangin. New Diffusion Phantoms Dedicated to the Study and Validation of HARDI Models. *Magn. Reson. Med.* **2008**, *60*, pp 1276–1283.

128. J.-D. Tournier, C.-H. Yeh, F. Calamante, K.-H. Cho, A. Connelly, and C.-P. Lin. Resolving Crossing Fibres Using Constrained Spherical Deconvolution: Validation Using Diffusion-Weighted Imaging Phantom Data. *Neuroimage* **2008**, *42*(2), pp 617–625.

129. E. Fieremans, Y. De Deene, S. Delputte, M. S. O. Zdemir, E. Achten, and I. Lemahieu. The Design of Anisotropic Diffusion Phantoms for the Validation of Diffusion Weighted Magnetic Resonance Imaging. *Phys. Med. Biol.* **2008**, *53*, pp 5405–5419.

130. P. Pullens, A. Roebroeck, and R. Goebel. Ground Truth Hardware Phantoms for Validation of Diffusion-Weighted MRI Applications. *J. Magn. Reson. Imaging* **2010**, *32*(2), pp 482–488.

131. A. Moussavi-Biugui, B. Stieltjes, K. Fritzsche, W. Semmler, and F. B. Laun. Novel Spherical Phantoms for *q*-Ball Imaging under *In Vivo* Conditions. *Magn. Reson. Med.* **2011**, *65* (1), pp 190–194.

132. P. Fillard, M. Descoteaux, A. Goh, S. Gouttard, B. Jeurissen, J. Malcolm, A. Ramirez-Manzanares, M. Reisert, K. Sakaie, F. Tensaouti, T. Yo, J.-F. Mangin, and C. Poupon. Quantitative Evaluation of 10 Tractography Algorithms on a Realistic Diffusion MR Phantom. *Neuroimage* **2011**, *56*(1), pp 220–234.

133. M. G. Hall and D. C. Alexander. Convergence and Parameter Choice for Monte-Carlo Simulations of Diffusion MRI. *IEEE Trans. Med. Imaging* **2009**, *28*(9), pp 1354–1364.

134. T. G. Close, J.-D. Tournier, F. Calamante, L. A. Johnston, I. Mareels, and A. Connelly. A Software Tool to Generate Simulated White Matter Structures for the Assessment of Fibre-Tracking Algorithms. *Neuroimage* **2009**, *47*(4), pp 1288–1300.

135. K. K. Seunarine, P. A. Cook, M. G. Hall, K. V. Embleton, G. J. M. Parker, and D. C. Alexander. Exploiting Peak Anisotropy for Tracking through Complex Structures, in *Mathematical Methods in Biomedical Image Analysis (MMBIA 2007)*, held in conjunture with the 11th International Conference on Computer Vision;2007, pp 1–8.

136. A. Goh, C. Lenglet, P. M. Thompson, and R. Vidal. Estimating Orientation Distribution Functions with Probability Density Constraints and Spatial Regularity, in *Proc. of the 12th International Conference on Medical Image Computing*

and Computer-Assisted Intervention: Part I; 2009, *LNCS*, vol. 5761, pp 877–885.

137. R. Duits and E. Franken. Left-Invariant Diffusions on the Space of Positions and Orientations and Their Application to Crossing-Preserving Smoothing of HARDI Images. *Int. J. Comput. Vis.* **2010**, *92*(3), pp 231–264.
138. M. Reisert and V. Kiselev. Fiber Continuity: An Anisotropic Prior for ODF Estimation. *IEEE Trans. Med. Imaging* **2011**, *30*(6), pp 1274–1283.
139. D. Fortin, C. Aubin-Lemay, A. Boré, G. Girard, J.-C. Houde, K. Whittingstall, and M. Descoteaux. Tractography in the Study of the Human Brain: A Neurosurgical Perspective. *Can. J. Neurol. Sci.* **2012**, *39*(6), pp 747–756.
140. M. Chamberland, K. Whittingstall, D. Fortin, D. Mathieu, and M. Descoteaux. Real-Time Multi-Peak Tractography for Instantaneous Connectivity Display. *Front. Neuroinform.* **2014**, *8*, p 59.
141. P. Hagmann, L. Cammoun, X. Gigandet, R. Meuli, C. J. Honey, V. J. Wedeen, and O. Sporns. Mapping the Structural Core of Human Cerebral Cortex. *PLoS Biol*. **2008**, *6*(7), p e159.
142. C. J. Honey, J.-P. Thivierge, and O. Sporns. Can Structure Predict Function in the Human Brain? *Neuroimage* **2010**, *52* (3), pp 766–776.
143. O. Sporns. The Human Connectome: Origins and Challenges. *Neuroimage* **2013**, *80*, pp 53–61.
144. M.-A. Côté, G. Girard, A. Boré, E. Garyfallidis, J.-C. Houde, and M. Descoteaux. Tractometer: Towards Validation of Tractography Pipelines. *Med. Image Anal.* **2013**, *17*(7), pp 857–844.
145. S. Farquharson, J.-D. Tournier, F. Calamante, G. Fabinyi, M. Schneider-Kolsky, G. D. Jackson, and A. Connelly. White Matter Fiber Tractography: Why We Need to Move beyond DTI. *J. Neurosurg.* **2013**, *118*(6), pp 1367–1377.
146. H. Johansen-Berg and T. E. J. Behrens. *Diffusion MRI*. Elsevier, 2009.
147. M. Catani and M. Thiebaut de Schotten. *Atlas of Human Brain Connections*. Oxford University Press, 2012.
148. M. Catani, D. K. Jones, and D. H. Ffytche. Perisylvian Language Networks of the Human Brain. *Ann. Neurol.* **2005**, *57*(1), pp 8–16.
149. M. Catani, R. J. Howard, S. Pajevic, and D. K. Jones. Virtual *In Vivo* Interactive Dissection of White Matter Fasciculi in the Human Brain. *Neuroimage* **2002**, *17*, pp 77–94.
150. G. Girard, K. Whittingstall, R. Deriche, and M. Descoteaux. Towards Quantitative Connectivity Analysis: Reducing Tractography Biases. *Neuroimage* **2014**, *98*(1), pp 266–278.
151. F. Pestilli, J. D. Yeatman, A. Rokem, K. N. Kay, and B. A. Wandell,(2014). Evaluation and statistical inference for human connectomes. *Nature Methods*, advance on. doi:10.1038/nmeth.3098
152. A. Daducci, A. Dal Palu, L. Alia, J.-P. Thiran, (2014). COMMIT: Convex Optimization Modeling for Micro-structure Informed Tractography. *IEEE Transactions on Medical Imaging*,PP(99), 1–1.doi:10.1109/TMI.2014.2352414
153. H. Duffau. Lessons from Brain Mapping in Surgery for Low-Grade Glioma: Insights into Associations between Tumour and Brain Plasticity. *Lancet Neurol*. **2005**, *4*(8), pp 476–486.
154. D. Leclercq, H. Duffau, C. Delmaire, L. Capelle, P. Gatignol, M. Ducros, J. Chiras, and S. Lehéricy. Comparison of Diffusion Tensor Imaging Tractography of Language Tracts and Intraoperative Subcortical Stimulations. *J. Neurosurg.* **2010**, *112*(3), pp 503–511.
155. Y. Iturria-Medina, R. C. Sotero, E. J. Canales-Rodríguez, Y. Alemàn-Gòmez, and L. Melie-García. Studying the Human Brain Anatomical Network via Diffusion-Weighted MRI and Graph Theory. *Neuroimage* **2008**, *40*, pp 1064–1076.
156. A. Anwander, M. Tittgemeyer, D. Y. von Cramon, A. D. Friederici, and T. R. Knosche. Connectivity-Based Parcellation of Broca's Area. *Cereb. Cortex* **2007**, *17*(4), pp 816–825.
157. M. Perrin, Y. Cointepas, A. Cachia, C. Poupon, B. Thirion, D. Rivière, P. Cathier, V. El Kouby, A. Constantinesco, D. Le Bihan, and J.-F. Mangin. Connectivity-Based Parcellation of the Cortical Mantle Using q-Ball Diffusion Imaging. *Int. J. Biomed. Imaging* **2008**, *2008*, pp 1–19.
158. L. Marrakchi-Kacem, C. Delmaire, A. Tucholka, P. Roca, P. Guevara, F. Poupon, J. Yelnik, A. Durr, J.-F. Mangin, S. Lehericy, and C. Poupon. Analysis of the Striato-Thalamo-Cortical Connectivity on the Cortical Surface to Infer Biomarkers of Huntington's Disease. *Med. Image Comput. Comput. Assist. Interv.* **2010**, *13*(Part 2), pp 217–224.
159. M. A. Koch, D. G. Norris, and M. Hund-Georgiadis. An Investigation of Functional and Anatomical Connectivity Using Magnetic Resonance Imaging. *Neuroimage* **2002**, *16*, pp 241–250.
160. M. Guye, G. J. M. Parker, M. Symms, P. Boulby, C. A. M. Wheeler-Kingshott, A. Salek-Haddadi, G. J. Barker, and J. S. Duncana. Combined Functional {MRI} and Tractography to Demonstrate the Connectivity of the Human Primary Motor Cortex *In Vivo*. *Neuroimage* **2003**, *19*, pp 1349–1360.
161. M. Guye, F. Bartolomei, and J.-P. Ranjeva. Imaging Structural and Functional Connectivity: Towards a Unified Definition of Human Brain Organization? *Curr. Opin. Neurol.* **2008**, *21*(4), pp 393–403.
162. F. D. Bowman, L. Zhang, G. Derado, and S. Chen. Determining Functional Connectivity Using fMRI Data with Diffusion-Based Anatomical Weighting. *Neuroimage* **2012**, *62*(3), pp 1769–1779.
163. P. Skudlarski, K. Jagannathan, V. D. Calhoun, M. Hampson, B. A. Skudlarska, and G. Pearlson. Measuring Brain Connectivity: Diffusion Tensor Imaging Validates Resting State Temporal Correlations. *Neuroimage* **2008**, *43*(3), pp 554–561.
164. C. J. Honey, O. Sporns, L. Cammoun, X. Gigandet, J. P. Thiran, R. Meuli, and P. Hagmann. Predicting Human Resting-State Functional Connectivity from Structural Connectivity. *Proc. Natl. Acad. Sci. USA* **2009**, *106*(6), pp 2035–2040.
165. K. Whittingstall, M. Bernier, J.-C. Houde, D. Fortin, and M. Descoteaux. Structural Network Underlying Visuospatial Imagery in Humans. *Cortex* **2014**, *56*(July), pp 85–98.
166. S. Smith. Introduction to the NeuroImage Special Issue "Mapping the Connectome." *Neuroimage* **2013**, *80*, p 1.

Maxime Descoteaux

Université de Sherbrooke, Québec, Canada